Basinwide Connections of Upper-Ocean Temperature Variability in the Equatorial Indian Ocean

GE SONG,[a,b] BOHUA HUANG,[c] RONGCAI REN,[a,d] AND ZENG-ZHEN HU[e]

[a] *State Key Laboratory of Numerical Modeling for Atmospheric Sciences and Geophysical Fluid Dynamics, Institute of Atmospheric Physics, Chinese Academy of Sciences, Beijing, China*
[b] *University of Chinese Academy of Sciences, Beijing, China*
[c] *Department of Atmospheric, Oceanic, and Earth Sciences and Center for Ocean–Land–Atmosphere Studies, College of Science, George Mason University, Fairfax, Virginia*
[d] *Collaborative Innovation Center on Forecast and Evaluation of Meteorological Disasters, Nanjing University of Information Science & Technology, Nanjing, China*
[e] *Climate Prediction Center, NCEP/NWS/NOAA, College Park, Maryland*

(Manuscript received 3 June 2020, in final form 1 March 2021)

ABSTRACT: In this article, the interannual variability of upper-ocean temperature in the equatorial Indian Ocean (IO) and its basinwide connections are investigated using 58-yr (1958–2015) comprehensive monthly mean ocean reanalysis data. Three leading modes of an empirical orthogonal function (EOF) analysis dominate the variability of upper-ocean temperature in the equatorial IO over a wide range of time scales. A coherent interannual band within the first two EOF modes identifies an oscillation between the zonally tilting thermocline across the equatorial IO in its peak phases and basinwide displacement of the equatorial thermocline in its transitional phases. Consistent with the recharge oscillation paradigm, this oscillation is inherent in the equatorial IO with a quasi-periodicity around 15 months, in which the wind-induced off-equatorial Rossby waves near 5°–10°S provide the phase-transition mechanism. This intrinsic IO oscillation provides the biennial component in the observed IOD variations. The third leading mode shows a nonlinear long-term trend of the upper-ocean temperature, including the near-surface warming along the equatorial Indian Ocean, accompanied by cooling trend in the lower thermocline originating farther south. Such vertical contrary trends may lead to an enhanced stratification in the equatorial IO.

KEYWORDS: Atmosphere; Indian Ocean; Interannual variability; Tropical variability

1. Introduction

Before the 1990s, the role of the ocean dynamics in the Indian Ocean interannual variability was not fully recognized and the equatorial Indian Ocean was regarded as a noninteractive ocean in this aspect (Wang 2019, among others). During the past two decades or so, more attention has been paid to the Indian Ocean's role in global climate variability and climate change (e.g., Webster et al. 1999; Schott and McCreary 2001; Annamalai and Murtugudde 2004). In depth investigations have been carried out on the ocean–atmosphere interactions and on the interannual and decadal variability in the Indian Ocean (Yamagata et al. 2004; Schott et al. 2009; Han et al. 2014; Xie et al. 2016).

For the interannual variability, there are two main patterns in the equatorial Indian Ocean, based on the empirical orthogonal function (EOF) analysis of the sea surface temperature anomalies (SSTAs) (e.g., Chu et al. 2014; Zhu et al. 2015). The first leading mode shows basinwide warming or cooling called the Indian Ocean basin mode (IOBM), which usually peaks in the early boreal spring and persists until the summer (Wu and Tang 2019). Statistically, the IOBM is highly correlated with the preceding El Niño–Southern Oscillation (ENSO) (e.g., Pan and Oort 1990; Kawamura 1994; Lanzante 1996; Nicholson 1997; Tourre and White 1997; Klein et al. 1999; Wang 2019). Consistently, late-decayed El Niño events in the recent decades are associated with interdecadal equatorial IO warming, which can persist into summer (Ren et al. 2015). Physically, the IOBM is mostly a response to the changed surface heat flux over the Indian Ocean induced by ENSO through the atmospheric bridge (e.g., Klein et al. 1999). Due to the Indian Ocean capacitor effect, the IOBM warming maintains the lingering El Niño influence on the Asian–Pacific region in the upcoming summer (e.g., Xie et al. 2002). In addition to interannual variations, the IOBM may also contain a significant warming trend (Allan et al. 1995; Terray and Dominiak 2005), possibly induced by anthropogenic climate change since the 1960s (Levitus et al. 2009).

The second leading mode is the Indian Ocean dipole (IOD) mode (e.g., Saji et al. 1999). Webster et al. (1999) and Saji et al. (1999) demonstrated that the IOD mode is characterized by SSTAs of opposite sign between the eastern and western equatorial Indian Ocean, which play an active role in regional and global climate on the seasonal and interannual time scales. Unlike the thermodynamic IOBM, the IOD is a dynamic mode (Huang and Kinter 2002). Although its coupled nature is generally recognized, there has been a great deal of disagreements about the triggering mechanisms of an IOD event (Allan et al. 1995). Some researchers argued that the dipole event is an inherent phenomenon of the Indian Ocean, even though it sometimes occur simultaneously with ENSO (Saji et al. 1999; Webster et al. 1999; Yamagata et al. 2004; Meyers et al. 2007). Others argued that the IOD is partly forced by the ENSO-induced zonal wind anomalies over the equatorial Indian Ocean (e.g., Klein et al. 1999; Huang and Kinter 2002). It is

Corresponding authors: Ge Song, songge@mail.iap.ac.cn; Rongcai Ren, rrc@lasg.iap.ac.cn

DOI: 10.1175/JCLI-D-20-0419.1

© 2021 American Meteorological Society. For information regarding reuse of this content and general copyright information, consult the AMS Copyright Policy (www.ametsoc.org/PUBSReuseLicenses).
Brought to you by NOAA Central Library | Unauthenticated | Downloaded 07/19/23 05:04 PM UTC

likely that the IOD events have multiple triggering sources. In a set of coupled simulations forced with observed SSTA outside the Indian Ocean, Huang and Shukla (2007a) reproduced many historical IOD events from 1958 to 1998. On the other hand, when the SST climatology is prescribed outside the Indian Ocean, summer deep convection over the northwestern Pacific can still trigger active IOD (Huang and Shukla 2007b). Similarly, Zhang et al. (2018) showed that the South China Sea summer monsoon is a potential trigger for the IOD.

There are fewer studies focusing on the subsurface variabilities (e.g., Feng et al. 2001; Rao et al. 2002; Wang 2019) than on the SST variabilities in the Indian Ocean (Saji et al. 1999; Webster et al. 1999; Venzke et al. 2000; Guo et al. 2018). Li et al. (2005) pointed out that anomalous wind on the surface of the central equatorial Indian Ocean is a major factor leading to the occurrence and development of the IOD. Fischer et al. (2005) proposed that the anomalous easterly winds along the equator stimulate upwelling Kelvin waves that reach the eastern coast rapidly. Then the wave spreads north and south as coastal Kelvin waves, shoaling the thermocline and cooling the SST over the eastern Indian Ocean, triggering an IOD event. The Bjerknes feedback further enhances the wind and SST anomalies, as well as the anomalous zonal gradient of the equatorial Indian Ocean thermocline (e.g., Chambers et al. 1999; Huang and Kinter 2002; Rao et al. 2002; Xie et al. 2002). At the same time, westward-propagating downwelling Rossby waves, excited by the anomalous wind stress curl located in the central-eastern basin near 5°–10°S, increase the depth of the thermocline. These off-equatorial thermocline anomalies propagate westward as Rossby waves (Masumoto and Meyers 1998), which suppress the Seychelles–Chagos thermocline ridge and warm up the SST over the southwestern Indian Ocean at a few months' lag (Huang and Kinter 2002; Xie et al. 2002; Jury and Huang 2004; Huang and Shukla 2007a). This delayed subsurface influence reduces the IOD growth and facilitates a switch from the IOD to the IOBM stage (Huang and Shukla 2007a).

Because the basic physical properties of the IOD are similar to those of ENSO, some researchers explained the mechanism of IOD with theories that are used to explain ENSO, such as the recharge oscillator (RO) paradigm (Jin 1997). RO has two basic features. 1) Since the phase speed of equatorial Kelvin waves is fast, the zonal wind stress anomalies are in equilibrium with the anomalous thermocline slope along the equator (Neelin 1991). 2) The cyclic nature of ENSO results from disequilibrium between the zonal mean equatorial thermocline depth and wind stress (e.g., Schneider et al. 1995). Meinen and McPhaden (2000) demonstrated that the equilibrium and disequilibrium modes are well represented by the first two EOF modes of the 20°C isotherm depth anomalies (D20) in the tropical Pacific, which they referred to as the tilt mode and the warm water volume (WWV) mode respectively (Clarke 2010; Kumar and Hu 2014). To represent the WWV mode succinctly, Meinen and McPhaden (2000) defined a WWV index as the spatial integration of D20 over 5°S–5°N, 120°E–80°W. In general, the WWV index is a good ENSO predictor because the increase of upper-ocean heat content is a prerequisite for El Niño (Wyrtki 1975; Cane and Zebiak 1985; Schneider et al. 1995; Hu et al. 2017).

The RO paradigm has been used to understand the equatorial variability in the other tropical oceans. Jansen et al. (2009) found that the equatorial Atlantic variability is well described by the RO model. Hu et al. (2013) showed that the two leading EOF modes of the vertical–longitude cross sections of the upper-ocean temperature anomalies in the equatorial Atlantic represent the WWV and tilt modes, respectively. However, results in the Indian Ocean seem to be mixed. Jansen et al. (2009) studied the IOD from the perspective of the RO theory but found the role of the heat content to be secondary. On the other hand, McPhaden and Nagura (2014) showed that the wind-forced Rossby waves in 5°–10°S are reflected at the western boundary into equatorial Kelvin waves at a sufficient lag from the ongoing IOD event, which facilitates its phase transition and generates a biennial character in the IOD mode. In general, the interannual variations of the upper-ocean heat content in the tropical Indian Ocean show a broad time scale from 2 to 5 years (Huang and Kinter 2002; McPhaden and Nagura 2014). However, this observed time scale seems to be determined partially by the external ENSO forcing. Whether the Indian Ocean has an intrinsic interannual oscillation and what constitutes its characteristic time scale need to be further analyzed.

The purpose of this study is to understand the nature of the interannual variability of the upper-ocean temperature in the equatorial Indian Ocean using a long dataset from a comprehensive ocean reanalysis. We focus on an objectively identified interannual oscillation of RO characteristics and analyze the evolution of heat content anomalies (HCAs), SSTAs, and wind anomalies at 10-m level during its life cycle. For this purpose, we first conduct an EOF analysis to identify the spatial and temporal patterns of the first three leading modes of the upper-ocean temperature anomalies in the equatorial Indian Ocean. Then, the physical processes of the equatorial variability related to the first two leading modes and their connections with atmospheric and oceanic variations in the Indian Ocean are investigated. A nonlinear long-term warming trend of the Indian Ocean identified from the third EOF mode is also analyzed. This paper is organized as follows. After the introduction, section 2 briefly introduces the reanalysis datasets used in this work. In section 3 we present the results, and a summary and discussion are given in section 4.

2. Data and methods

The monthly ocean temperature data of the Ocean Reanalysis System 4 (ORAS4) from January 1958 to December 2015, produced by the European Centre for Medium-Range Weather Forecasts (ECMWF) (Balmaseda et al. 2013), are used in this analysis. The horizontal grid spacing is 1° latitude × 1° longitude, which is interpolated from the original grid. There are 20 vertical levels of about 10-m level thickness in the upper 315 m and 42 levels above 5350 m. The SSTA and upper-ocean HCA (defined as the mean ocean temperature anomalies of the upper 315 m multiplied by the density and the specific heat of seawater) from 1958 to 2015 are also examined. The datasets of monthly mean zonal and meridional winds at 10-m level for 1958–2015 are from the National Centers

Brought to you by NOAA Central Library | Unauthenticated | Downloaded 07/19/23 05:04 PM UTC

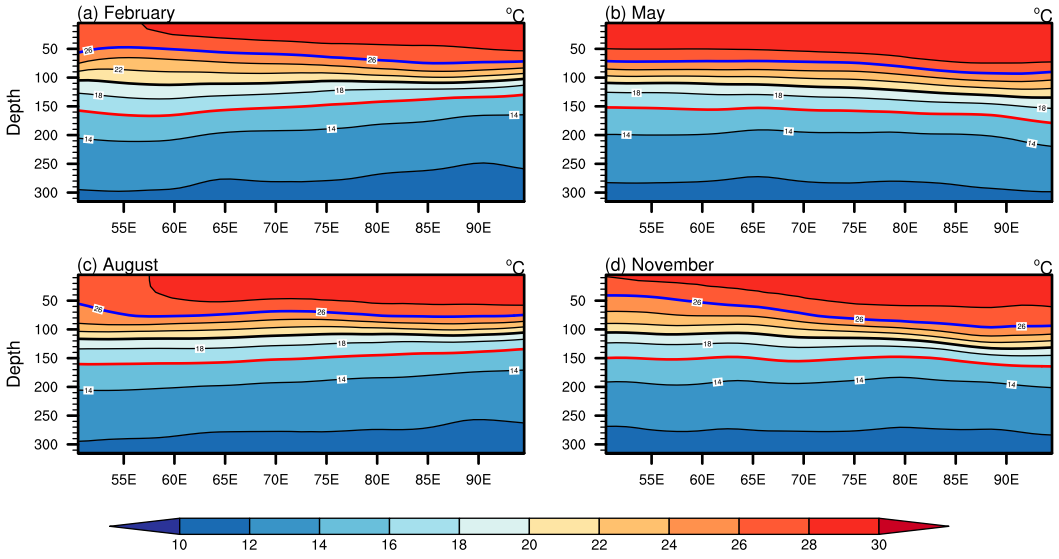

FIG. 1. Longitude–depth cross sections of the upper-ocean temperature monthly climatology in the equatorial Indian Ocean (0–315 m, 50°–95°E, and averaged over 2°S–2°N) for (a) February, (b) May, (c) August, and (d) November. The climatology is calculated using the monthly data from January 1958 to December 2015. The contour interval is 2°C with the thick blue, black, and red lines showing the 26°, 20° (D20), and 16°C isotherms.

for Environmental Prediction (NCEP)–National Center for Atmospheric Research (NCAR) Reanalysis (Kalnay et al. 1996), which was downloaded from https://psl.noaa.gov/data/gridded/data.ncep.reanalysis.derived.surfaceflux.html.

Following Hu et al. (2013), an EOF analysis is conducted on the upper-ocean temperature anomalies from January 1958 to December 2015 averaged between 2°S and 2°N and distributed at 20 levels from 0 to 315 m. Considering the uneven distribution of the vertical levels, the data at each level are weighted by the square root of its corresponding layer thickness before constructing the covariance matrix for the EOF analysis. In this study, traditional spectral analysis such as the fast Fourier transform (FFT) method is used to identify periodic components in the PCs. The original periodograms of detrended PCs are smoothed utilizing modified Daniell smoothing of length 5. However, the traditional spectral analysis starts with prescribed basis functions and the window functions used in these methods for smoothing spectral estimates are subjectively chosen which would also contribute to distortion of spectra (Padmanabhan and Rao 1986; Wu and Shen 2016). To overcome these issues, the empirical mode decomposition (EMD) was introduced as a part of the Hilbert–Huang transform (Huang et al. 1998). The EMD method extracts oscillatory intrinsic mode functions (IMFs) from the data by utilizing local minima and maxima, so it is an adaptive filter in nature. To overcome the mode mixing problem of EMD, Wu and Huang (2009) later developed ensemble empirical mode decomposition (EEMD) analysis, which adds multiple noise realizations to the observed time series before the decompositions and derive ensemble averaged IMFs (Wu and Huang 2009). The EEMD technique based on the local characteristic time scales of the data itself, without introducing a priori basis functions. The effectiveness of EEMD has been applied widely in geophysical fields (Huang and Wu 2008; Wu and Huang 2009; Feng et al. 2014) and it is superior to traditional spectral analysis in extracting the annual cycle components from climate variable (Wu et al. 2007; Qian et al. 2011). Thus we further take advantage of the EEMD analysis to investigate the annual cycle components from the original principal component (PC).

Several climate indexes are used in this study. The ENSO signal is represented by the Niño-3.4 index, defined as the averaged SSTA over 5°S–5°N, 120–170°W (Barnston et al. 1997). The definition of dipole mode index (DMI) follows (Saji et al. 1999) as the difference in the averaged SSTA between the western (10°S–10°N, 50°E–70°E) and southeastern (10°S–10°N, 90°–110°E) tropical Indian Ocean. When the DMI is positive, the phenomenon is referred to as the positive phase of IOD; when it is negative, it is referred to as the negative phase of IOD. The IOBM index is defined as the averaged SSTA in 20°S–20°N, 40°–110°E (Yang et al. 2007).

3. Results

As a background for the discussion of the interannual variability of upper-ocean temperature along the equatorial Indian Ocean (IO), we briefly summarize the basic features of the mean state and seasonal cycle. The major part of the equatorial IO can be regarded as a portion of the Indo-Pacific warm pool, where SST is higher than 28°C (Feng and Meyers 2003). Unlike the Pacific Ocean, there is no cold tongue in the eastern tropical Indian Ocean where SST near the Sumatra coast is even warmer than that near the western boundary. The equatorial thermocline zone is roughly in the temperature range of 16°–26°C marked by red and blue curves respectively (Fig. 1). We use D20 (thick black curve) shown in Fig. 1 to characterize the mean thermocline depth, which is nearly flat along the equator

Brought to you by NOAA Central Library | Unauthenticated | Downloaded 07/19/23 05:04 PM UTC

at depth slightly deeper than 100 m. On the other hand, isotherms near the top of the thermocline (e.g., 26°C; blue curve) tilt up slightly westward in the central and western Indian Ocean in most of the seasons.

In response to monsoonal winds, the Indian Ocean exhibits a unique seasonal cycle (Schott et al. 2009). During the summer monsoon season, southerly alongshore winds cause pronounced upwelling in the western Indian Ocean and enhance the upward tilting of the upper-ocean isotherms (Fig. 1c). Seasonal upwelling also occurs off the coasts of Java and Sumatra during boreal summer and is weakened during winter season, but it is hardly observed in Fig. 1 due to the spatial averages of temperature in 2°S–2°N. Interannual fluctuation of the upwelling in the eastern IO may be an important trigger of IOD events. Another unique feature is the prevailing semiannual westerly winds on the equator during intermonsoon transitions (e.g., May and November; not shown) although the thermocline is nearly flat in these months (Figs. 1b,d). In response, strong eastward equatorial currents appear twice per year. Referred to as the Wyrtki jets after the discoverer (Wyrtki 1973), these currents deepen the thermocline near the eastern Indian Ocean and suppress the seasonal upwelling there. Measured by D20, the seasonal variation of the depth of the equatorial thermocline is not obvious. In this work, we focus on the interannual time scale variabilities in the upper ocean, and the relevant physical processes.

a. *Leading modes of the upper-ocean temperature variability*

Figure 2 shows the first three leading EOF modes of the monthly anomalies of the upper-ocean temperature and the corresponding principal components, which together explain over 70% of the total variance. North's rule of thumb for distinction indicates that the eigenvalues of EOFs 1–3 are statistically separated (North et al. 1982). The spatial pattern of EOF1 (Fig. 2a), which accounts for 42.6% of the total variance, depicts opposite fluctuations between the eastern and western equatorial Indian Ocean, presenting an east–west ocean temperature dipole-like variation in the equatorial subsurface ocean. On average, the subsurface ocean temperature variabilities in the eastern equatorial IO are stronger than those in the western equatorial IO. The depths of the location of the ocean temperature variation center in the eastern and western equatorial IO are at about 100 m where the climatological thermocline is located (see the green dashed line in Fig. 2a). Therefore, this EOF mode corresponds to an enhanced upward (downward) tilt of the equatorial thermocline toward the east when PC1 is positive (negative). One should also note that similar EOF1 patterns have been derived for the equatorial Pacific Ocean (Kumar and Hu 2014) and the equatorial Atlantic Ocean (Hu et al. 2013). These previous studies have referred to this pattern as the tilt mode (Clarke 2010; Kumar and Hu 2014), representing the equilibrium state in the RO paradigm (Jin 1997).

PC1 exhibits dominant variability on an interannual time scale (Fig. 2d). Its power spectrum shows near red noise distribution from the subannual to interannual band with statistically significant subannual, near-annual, and near-biennial peaks above the 95% confidence level (Fig. 3a). On the other hand, there exists a mild trend as more noticeable negative episodes occurred after the 1970s (Fig. 2d). PC1 is correlated with the SSTA in the IO and the other oceans, especially the IOD and ENSO-like patterns (Fig. 4a). When PC1 lags DMI by 1 month, their statistically significant correlation coefficient reaches a maximum of 0.33 (not shown). Since the subsurface temperature anomalies are stronger than those at the surface (Fig. 2a), the SSTA associated with IOD is likely a surface manifestation of the subsurface thermocline adjustment (Tan et al. 2003). The correlation between PC1 and the Niño-3.4 index is also statistically significant and up to 0.32 when there is no lag (not shown), indicating a simultaneous correlation of the PC1 with ENSO. It should be pointed out that EOF1 does not exclusively represent the IOD and PC1 is only moderately correlated with both ENSO and IOD indices.

The EOF2 (Fig. 2b) accounts for 16.4% of the total variance. It also shows an out-of-phase variation between the western and eastern IOB. Compared with EOF1, its negative loading is greatly weakened, while its positive loading is enhanced and extends eastward. West of 75°E, the maximum loading is located near the mean thermocline around 100 m (green dashed curve, Fig. 2b). In the eastern IO, the negative loading lies above the mean thermocline while the positive loading lies below, indicating the out-of-phase variation of temperature across the thermocline. It is further noticed that the opposite anomalies in the upper and lower thermocline are asymmetric, with the lower thermocline anomalies dominating. Therefore, in the positive (negative) episodes of PC2 (Fig. 2e), the thermocline deepens (shoals) in the equatorial IO and the thermocline zone in the east becomes much wider (narrower). We hypothesize that the EOF2 is an analog to the WWV mode of the RO paradigm, which presents a more complicated structure than the EOF patterns of WWV in the equatorial Pacific (Kumar and Hu 2014, their Figs. 4c and 4d) and Atlantic (Hu et al. 2013, their Fig. 3c). Hu et al. (2013) showed that the WWV mode in the equatorial Atlantic represents a deepening (shoaling) of the equatorial thermocline throughout the basins. Different from PC1, PC2 has a weak correlation with the SSTAs in the tropical Indian and Pacific Oceans (Fig. 4b). The maximum correlations between PC2 and SSTA are present off the equator.

PC2 shows not only a substantial amount of variation in the interannual time scales but also significant low-frequency fluctuations (Fig. 2e). For example, prolonged positive phases occurred during 1958–68 and 2006–15; negative ones occurred in 1969–78 and 1999–2006 (Fig. 2e). Different from PC1, the spectrum of PC2 is nearly white from annual to interannual frequencies because PC2 contains a variety of different frequency fluctuations. However, the power spectrum of PC2 shows a peak at the period of about 10 months and minor peaks at periods of about 1.5 and 4 years (Fig. 3b). Consistent with our visual observations of Fig. 2e, the most significant periods in the spectrum are more than 10 years, suggesting that it contains multidecadal to decadal variability (Fig. 3b).

The third leading mode (EOF3) accounts for 12.0% of the total variance (Fig. 2c) with major loading in the upper 150 m. The loadings of EOF3 above 100 m are basically of the same sign, indicating a coherent ocean temperature variation that

Brought to you by NOAA Central Library | Unauthenticated | Downloaded 07/19/23 05:04 PM UTC

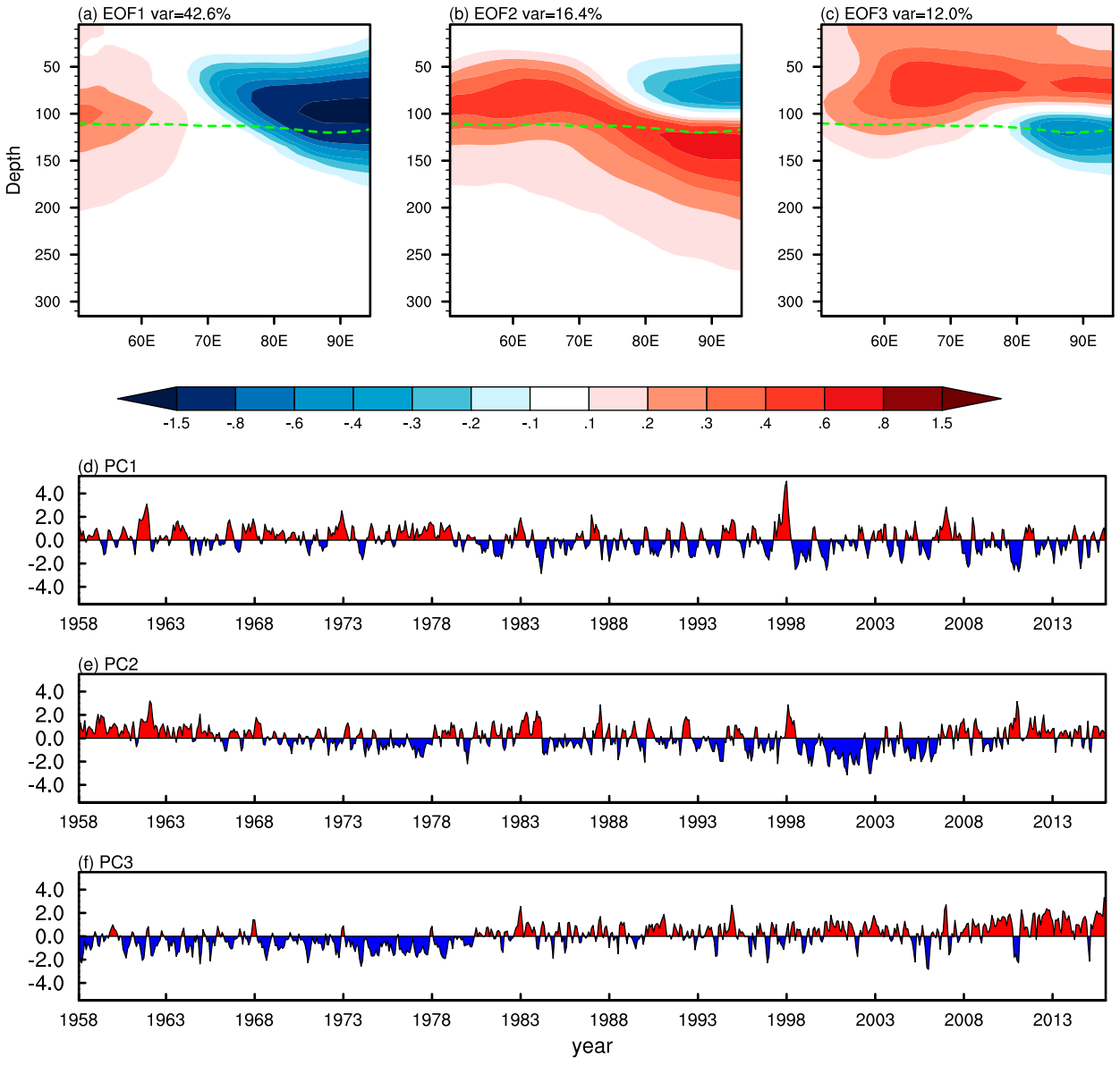

FIG. 2. The (a) EOF1, (b) EOF2, and (c) EOF3 of the upper-ocean temperature anomalies (0–315 m, 50°–95°E, and averaged over 2°S–2°N) along the equatorial Indian Ocean, and their corresponding normalized (d) PC1, (e) PC2, and (f) PC3. The unit of the EOFs is °C. The thick green dashed lines in (a)–(c) are the climatological mean D20.

includes that of the oceanic mixed layer (OML) but extends deeper. An area of the opposite sign is located at the depth of 110–140 m in the eastern IO. Such a spatial pattern of EOF3 (Fig. 2c) suggests that as the OML is warmed up, the upper thermocline is also warmed while the lower thermocline cools down in the east. In addition to substantial interannual fluctuations, PC3 (Fig. 2f) stands out with a long-term upward trend, signifying that the OML is warming up significantly throughout the whole period. From Fig. 4c, we can see that PC3 and SSTA are positively correlated across the whole IO basin. This is consistent with a statistically significant correlation coefficient between PC3 and IOBM index of 0.37 (not show). The power spectrum of PC3 (Fig. 3c) is similar to that of PC2 (Fig. 3b), with near white-noise bands from the subannual to interannual range. Against the red noise background, there are two significant bands around subannual and decadal frequencies (Fig. 3c). The interannual variations, however, are relatively weak.

b. The equatorial Indian Ocean oscillation

Next, we examine whether there are oscillatory and propagating modes in the interannual variations. In general, a propagating mode cannot be characterized by one EOF mode. However, although the simultaneous correlation coefficients

Brought to you by NOAA Central Library | Unauthenticated | Downloaded 07/19/23 05:04 PM UTC

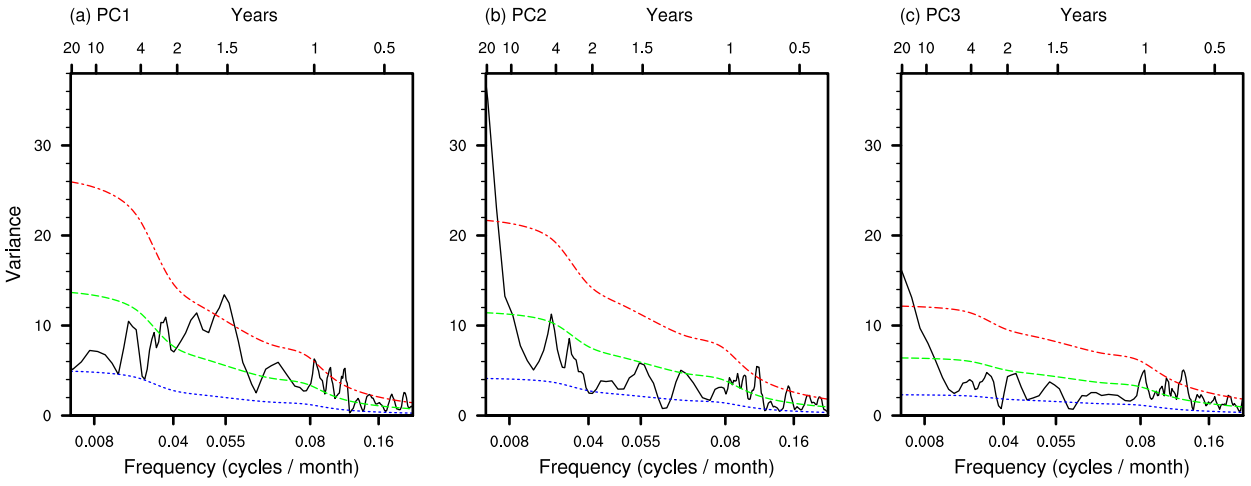

FIG. 3. Power spectrum of normalized (a) PC1, (b) PC2, and (c) PC3 (black line) from which the linear trend is removed. The corresponding "red noise" curve (green line) and the curves indicating the 5% and 95% confidence bounds (blue and red line) are also plotted.

among PCs are zero due to the orthogonality of the EOF technique, the lead–lag correlations between PC1 and PC2 show the maximum correlation coefficient of 0.40 when the PC1 leads PC2 by two months (Fig. 5a). On the other hand, there are no significant lead–lag correlations between PC1 and PC3 and between PC2 and PC3 (not shown). The time lag between PC1 and PC2 indicates that, starting from the stage when the cold ocean temperature anomalies prevail in the eastern IO (EOF1), the subsurface warm anomalies over the western IO shown in EOF1 may spread eastward with time. After about a couple of months, they are likely to occupy the entire equatorial IO in depth between 100 and 200 m. As a result, the original strong negative anomalies over the eastern Indian Ocean will be greatly weakened and EOF2 pattern emerges. It means that EOF2 may be the next stage following EOF1. Therefore, we speculate that these two EOF modes may be connected through the RO paradigm.

The maximum lead–lag correlation between PC1 and PC2 (Fig. 5a) is smaller than the corresponding one in the equatorial Pacific (Fig. 3d; Kumar and Hu 2014). This may be because there is no single dominant variability in the equatorial IO such as that in the equatorial Pacific Ocean associated with ENSO. As a result, each EOF mode contains multiple signals of the interannual to decadal time scales although the coherent variations between EOF1 and EOF2 may exist mainly on the interannual time scale. Although it is possible to specify the dominant period of a time series using spectral analysis, this method is limited to an a priori stationary structure, such as a sine curve, ignoring the nonlinearity and nonstationarity of climate variations (Qian et al. 2011; Wu and Shen 2016). Therefore, it seems necessary to separate signals of the PCs into those with different time scales using EEMD analysis. As previously mentioned, EEMD is an adaptive time series analysis technology developed in recent years, which is suitable for analyzing nonlinear and nonstationary time series such as climate data (Wu and Huang 2009). It should be pointed out that the traditional methods of spectral analysis have some

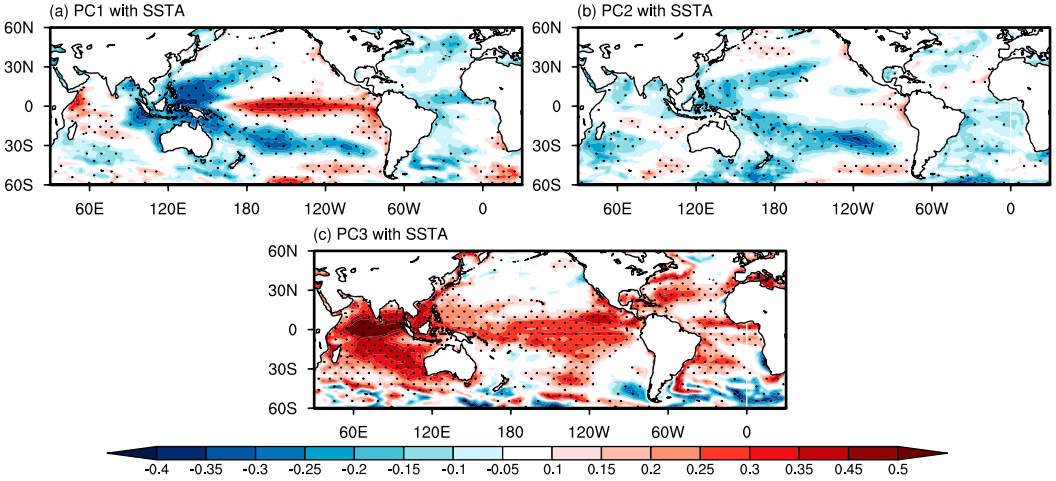

FIG. 4. The correlations of (a) PC1, (b) PC2, and (c) PC3 with global SSTA in January 1958–December 2015. Dotted areas indicate that the correlations are statistically significant above the 95% confidence level.

Brought to you by NOAA Central Library | Unauthenticated | Downloaded 07/19/23 05:04 PM UTC

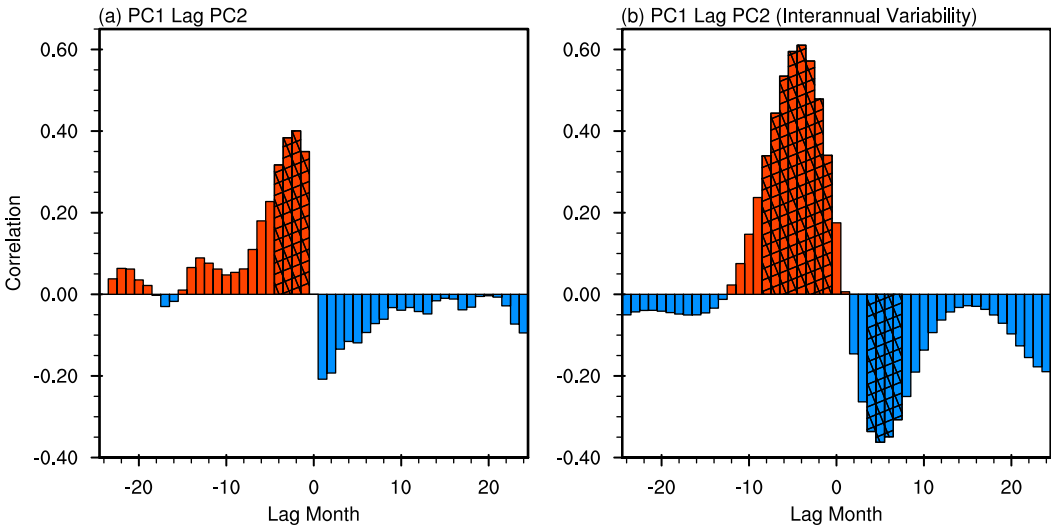

FIG. 5. Lead–lag correlations (a) between PC1 and PC2 and (b) between the interannual variability of PC1 and PC2. Hatched areas indicate that the correlation coefficients are statistically significant above the 95% confidence level. Positive (negative) numbers of the x axis represent the months that PC1 lags (leads) PC2.

disadvantages such as poor resolution, a priori stationary basis functions, and subjective choice of amount of smoothing (Padmanabhan and Rao 1986; Qian et al. 2011). These limitations may cause some discrepancies between the periods obtained by spectral analysis and EEMD analysis (Ren and Liu 2018). Following Huang et al. (2012) and Feng et al. (2014), we perform an EEMD analysis on all three PCs separately and obtained nine oscillatory modes (IMFs 1–9) from high to low frequency and a long-term trend (IMF10) for each PC.

As an example, Fig. 6 shows the IMFs and nonlinear trend from PC1. It can be seen that PC1 is succinctly decomposed to components of different variations from the subannual to interannual to interdecadal time scales. The subannual signals include vigorous variations on time scales of 3–4 months (IMF1; Fig. 6a) and 7–8 months (IMF2; Fig. 6b). Physically, IMF1 corresponds to near 90-day fluctuation along the southern coast of Sumatra and Java (Iskandar et al. 2005) whereas IMF2 is associated with the stronger semiannual variability. Both are well-known dynamical variations in the equatorial IO. Sengupta et al. (2007) suggest that there is an intrinsic 90-day time scale in the equatorial IO arising from wave adjustment. On the other hand, Han et al. (2011) argue that dominant signals at 90-day and semiannual (180-day) periods represent basin resonances in response to fluctuating wind forcing. In both scenarios, these subannual signals are dominated by active equatorial waves. The interannual signals are composed of near-annual (IMF3; Fig. 6c) and 3- and 5-yr (IMF4 and IMF5; Figs. 6d,e) variations. The near-annual band is most active and continuous whereas IMF4 is more intermittent with large peaks occurring in the major El Niño winters (e.g., 1972–73, 1982–83, and 1997–98). IMF5 is apparently weaker than the other two. The interdecadal band, composed of the rest of the fluctuating IMFs, has a characteristic time scale of 10–12 years and generally weaker amplitude than the interannual modes (Fig. 6f). The last IMF (Fig. 6g) shows a monotonic weak decreasing trend, which is also visible in the original PC1 (Fig. 2d). These EEMD components of PC1 correspond largely to the distribution of its power spectrum (Fig. 3a). The EEMD decompositions of PC2 and PC3 yield similar results, although the intensities of different frequency bands vary (not shown).

We have examined the lead–lag correlations between PC1 and PC2 with respect to their subannual, interannual, and interdecadal bands. For the EEMD-isolated interannual time scale variations only (sum of IMFs 3–5), the maximum lag correlation between PC1 and PC2 increases to 0.60 and occurs when PC1 leads PC2 by 5 months (Fig. 5b). Further examining each of the three interannual-time-scale components (IMFs 3, 4, and 5) of PC1 and PC2 suggests that only the IMF3s of PC1 and PC2 show a coherent oscillatory relationship with a steady phase difference although the amplitude of the PC1's IMF3 is generally larger (Fig. 7a). The power spectrum analysis confirms that the two IMF3s have a similar spectral period at around 15 months (not shown). The maximum of lead–lag correlation coefficient reaches 0.67 for their IMF3s when PC1 leads PC2 by 4 months. Therefore, we argue that the coherent variability as depicted by PC1 and PC2 is an oscillation on this particular time scale, which we refer to as the equatorial IO oscillation.

To further examine the evolution within the oscillation cycle, we conducted a phase-based composite analysis (Lau and Lau 1990; Moron et al. 1998; Huang and Kinter 2002). For this purpose, we first reconstructed the filtered spatial-temporal fields of the ocean temperature anomalies by summing up the IMF3 components of PC1 and PC2, each multiplied with its corresponding EOF mode, respectively. The IMF3 of PC3 contains a much weaker signal on this frequency band and is not counted in the reconstruction. Following the procedure of Moron et al. (1998), a new EOF analysis is conducted on the reconstructed field and its first normalized PC, denoted as $c(t)$, is used as the index to represent the equatorial IO oscillation. Shown as the red curve in Fig. 7b, $c(t)$ demonstrates very

Brought to you by NOAA Central Library | Unauthenticated | Downloaded 07/19/23 05:04 PM UTC

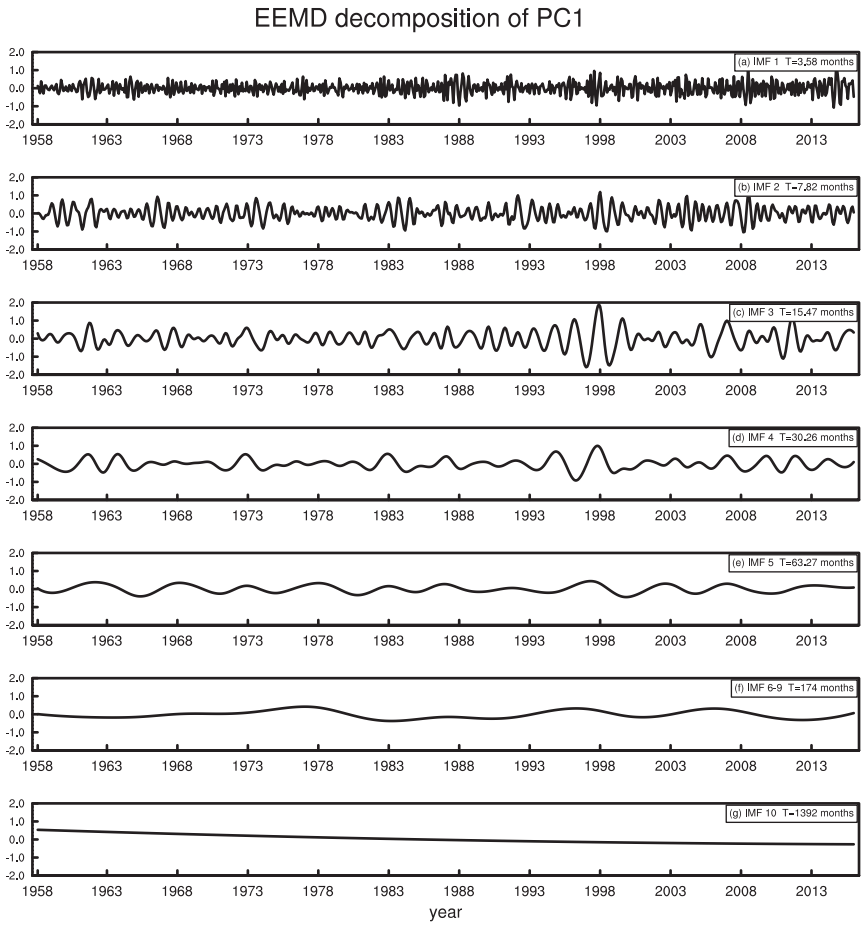

FIG. 6. The EEMD decompositions of PC1: (a) IMF1, (b) IMF2, (c)–(e) IMFs 3–5 (interannual time scales), (f) IMFs 6–9, and (g) IMF10 (trend). The period (unit: months) of each component is shown in the upper-right corner.

similar oscillatory characteristics to the IMF3s of PC1 and PC2 as shown in Fig. 7a. Its power spectrum also shows a significant period around 15 months (Fig. 7c).

The amplitude $A(t)$ and phase $\theta(t)$ of this oscillation can be obtained from the following complex equation as $c'(t) + ic(t) = A(t)\exp[i\theta(t)]$, where $c'(t)$ (dashed blue curve, Fig. 7c) is the normalized time derivative of $c(t)$ (Moron et al. 1998). Figure 8 shows the time series of $A(t)$ (Fig. 8a) and $\theta(t)$ (Fig. 8b). It can be seen that the amplitude of the oscillation is variable and peaked around 1998 (Fig. 8a) while its phase varies cyclically in the range of $-180°$ and 180°. For a complete cycle, its phase increases nearly monotonically from $-180°$ to 180°, even though the period of each cycle is somewhat variable. Operating in the near-annual to biennial frequency band, the oscillation seems quite continuous, except for a few interruptions, such as those in 1963, 2004, and 2013 (Fig. 8b).

The phase-based composite is constructed using both the instant phase and amplitude as shown in Fig. 8 with the following procedure. First, every identified full cycle with increasing phase from $-180°$ to 180° is evenly divided into eight subphase intervals of 45° each. For example, subphase 1 is defined as $-180° \le \theta(t) \le -135°$. Then data samples from all full cycles that fall in a given subphase are selected to form the composite of that subphase, as long as the sample's instant amplitude is greater than a given threshold [$A(t) > 0.8$]. As a result, for any variable, we can get a sequence of eight composites that characterize the evolution of the full life cycle in the equatorial IO oscillation. Usually, half of the life cycle is displayed with four subphase composites because the other four composites are nearly mirror images with opposite signs. From the composites of the four chosen consecutive phases (referred to simply as 1, 2, 3, and 4 hereafter), we can see the composite life cycle of this oscillation.

Figure 9 shows the composite evolution of the upper-ocean temperature anomalies in the equatorial IO for the four consecutive phases, which corresponds to a half of the life cycle. In phase 1, established cold temperature anomalies in the eastern IO peak while the warm anomalies in the west continue to accumulate and expand eastward (Figs. 9a,b). In phase 2, a well-developed asymmetrical tilting pattern with the cold anomalies in the east and warm anomalies in the west is formed (Fig. 9b), similar to EOF1 (Fig. 2a). From phase 2 to 3 (Figs. 9b,c), both

Brought to you by NOAA Central Library | Unauthenticated | Downloaded 07/19/23 05:04 PM UTC

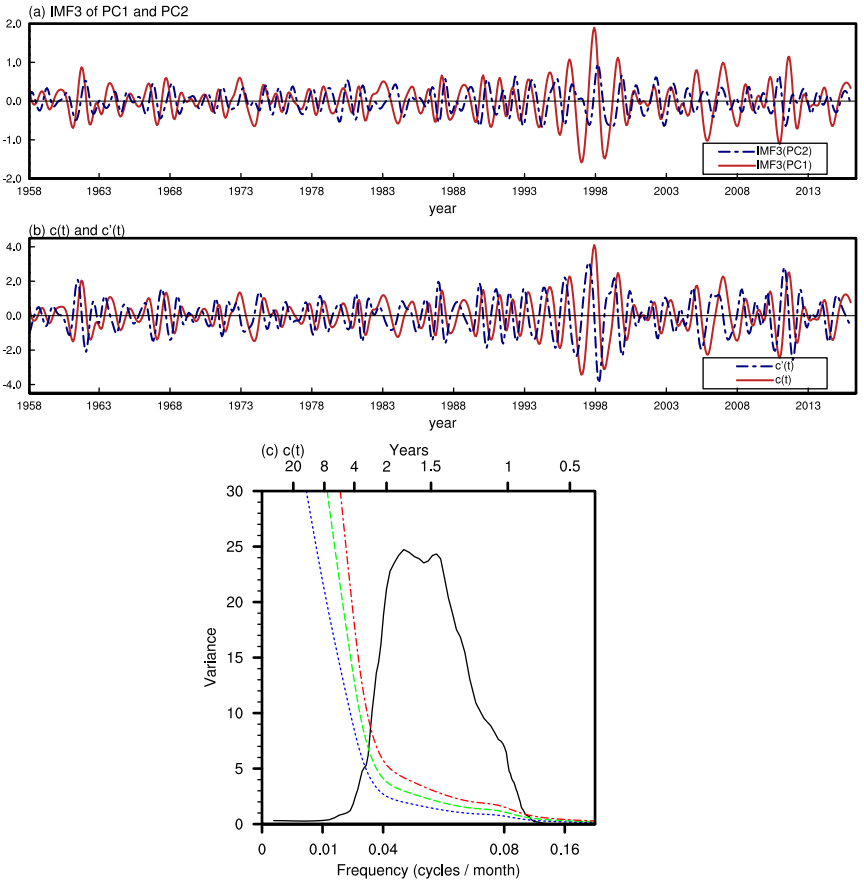

FIG. 7. The time series of (a) IMF3 of PC1 (red solid line) and PC2 (blue dashed line) and (b) $c(t)$ (red solid line) and $c'(t)$ (blue dashed line). (c) The spectrum of $c(t)$ (black line) and the corresponding "red noise" curve (green line) and the curves indicating the 5% and 95% confidence bounds (blue and red line).

the warm anomalies in the west and cold anomalies in the east (i.e., the tilt mode) weaken somewhat. The cold anomalies in the east decay faster as the lower thermocline is warmed up (Fig. 9c). In phase 4, the cold anomalies in the eastern Indian Ocean disappear while warm anomalies spread throughout the basin with maximum in the east (Fig. 9d). This structure represents a general deepening of the equatorial thermocline, corresponding to a state of maximum WWV in the basin. It preconditions the opposite tilt pattern to develop in the next phase. The evolution of the composites demonstrates the development of the equatorial oscillation between the tilt and WWV states following the RO paradigm.

The corresponding HCA composites in these four phases (shading in Fig. 10) show the basinwide thermocline variations associated with the equatorial IO oscillation. Also plotted on Fig. 10 are the wind anomalies (vectors) at the 10-m level. In phase 1 (Fig. 10a), cold HCAs are in the east and warm HCAs in the west along the equator, signifying the anomalous eastward tilt of the thermocline. Correspondingly, equatorial easterly wind anomalies prevail throughout the basin (vectors in Fig. 10a), which maintain the Sverdrup balance along the equator (Philander 1990). This quasi-equilibrium also persists to phase 2 (Fig. 10b). In the meantime, the jetlike anomalous easterly winds in phase 1 and 2 (vectors in Figs. 10a,b) generate Ekman pumping on both sides of the equator and the off-equatorial positive HCAs in the midbasin (shading in Figs. 10a,b). An asymmetry of the off-equatorial HCAs appears between the north and south partly because of the barrier effect of the Indian subcontinent in the north. More important, however, is the contemporary weakening of the southeast trade winds in the central basin, which, together with the equatorial easterly anomalies, enhances the anticyclonic wind curl and extends it southward. As a result, the HCAs are strengthened near 5°–10°S, and propagate westward as slower Rossby waves, deepening the thermocline in the western IO (Fig. 10b). In phase 3 (Fig. 10c), the negative HCAs are weakened in the eastern IO, possibly due to the eastward propagation of the positive HCAs along the equator. We hypothesize that the westward-propagating off-equatorial Rossby waves are reflected into equatorial Kelvin waves at the western boundary. Furthermore, the related weakening of the equatorial easterly anomalies may also contribute to weakening of the negative HCAs in the east. However, since the equatorial Kelvin waves cross the basin in about 30 days (e.g., Sengupta et al. 2007), its propagation is not

Brought to you by NOAA Central Library | Unauthenticated | Downloaded 07/19/23 05:04 PM UTC

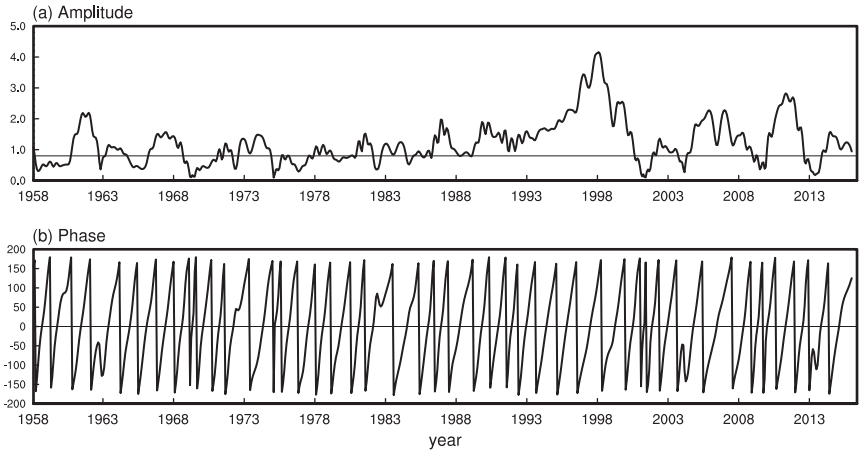

FIG. 8. The (a) amplitude and (b) phase derived from the new PC1 [$c(t)$] and its time derivative [$c'(t)$]. The unit of phase is degree and the straight line in (a) shows the amplitude criteria for composites.

as discernable as the off-equatorial Rossby waves in the sequence of composites. It is interesting to note that the initial influence of the oceanic Kelvin waves seems to warm up the lower thermocline in the eastern equatorial IO (Fig. 9c). As ocean heat is persistently transported into the equatorial zone in the west and then carried to the east, the thermocline is deepened in the equatorial east Indian Ocean (Fig. 10d), which leads to the switch to the negative episode of the oscillation. Eventually, opposite sign variations appear with a similar evolution to complete the life cycle. One should also notice that, as an equatorial Kelvin wave hits the eastern boundary, it propagates along the boundaries poleward in the form of coastal Kelvin waves (Gill 1982). Part of the wave also propagates westward as the reflected equatorial Rossby waves, at phase speeds decreasing with latitudes. These features can be traced through the sequence of the cold HCAs in the eastern Indian Ocean (Fig. 10). Since the reflected Rossby wave propagates more slowly, it is damped more than the eastward-propagating Kelvin wave. Therefore, the reinforcement by the wind curl–induced HCAs en route is critical to ensure that the off-equatorial waves reaching the western boundary still have substantial strength.

Corresponding composites for SSTA in the Indian Ocean show a largely consistent surface evolution. In interpreting the SSTA patterns, one should keep in mind that the SSTA is driven by subsurface temperature anomalies mainly in the upwelling areas (Zhang and Han 2020), which are largely confined in the equatorial waveguide, the coastal zones, and

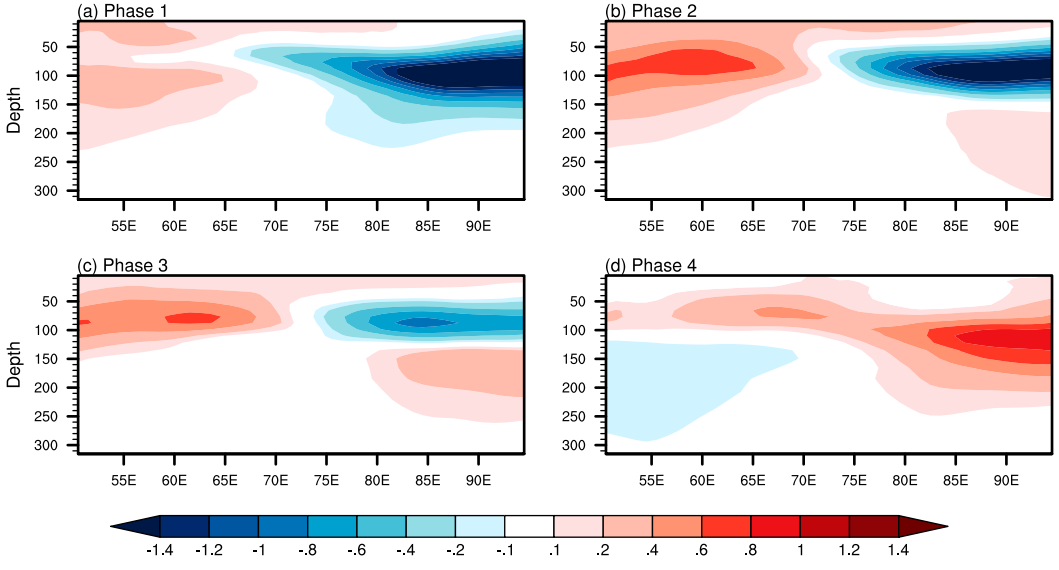

FIG. 9. Longitude–depth cross sections of upper-ocean temperature anomalies composites averaged over 2°S–2°N cross the Indian Ocean in phases (a) 1, (b) 2, (c) 3, and (d) 4. The unit is °C.

Brought to you by NOAA Central Library | Unauthenticated | Downloaded 07/19/23 05:04 PM UTC

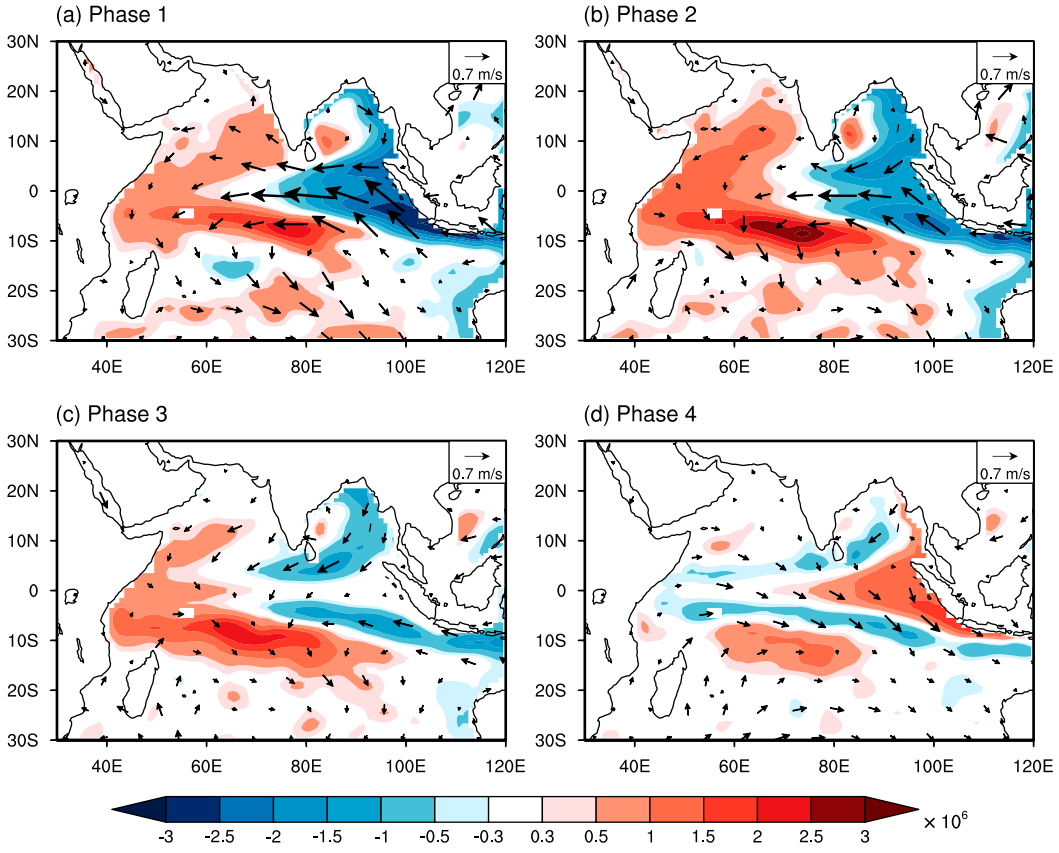

FIG. 10. The heat content anomaly (HCA; shading) and 10-m wind anomalies (vectors) composites in phases (a) 1, (b) 2, (c) 3, and (d) 4. The unit is m s^{-1} for the 10-m wind and J m^{-2} for HCA.

the Seychelles–Chagos thermocline ridge. Outside these areas, surface heat flux anomalies may also play an important role. This is why the SSTA is distributed more broadly than HCA. When negative subsurface temperature anomalies develop in the eastern equatorial IO, they force the negative SSTAs locally and along the coast of Sumatra (not shown). Because of the Bjerknes feedback, the anomalous zonal SST gradient along the equator enhances the easterly anomalies, which in turn induce deepening of the thermocline in the eastern equatorial IO. This feedback pattern is most clearly seen in the first stage (Fig. 11a). The negative SSTAs near the coast of Sumatra in the eastern equatorial IO peak when the thermocline shoals there and the equatorial eastern wind anomalies prevail (Figs. 9a and 10a), while the warm SSTAs are still weak in the west. By the second stage, as the thermocline deepens from the central to western equatorial IO, warm SSTAs enhance and extend eastward while the negative SSTAs in the east are weakened and largely off the equator (Fig. 11b). Moreover, warm SSTAs also extend to the southeast. In addition to the somewhat quicker demise of the negative SSTAs in the eastern equatorial IO, the southeastward extension of the warm SSTAs (Fig. 11) gives a somewhat different surface structure from the subsurface thermal pattern (Figs. 9 and 10). We have found that the warm SSTAs extended to the southeast tropical IO are mainly forced by the surface latent heat flux anomalies associated with the weakened trade winds while the equatorial SSTAs are generated by ocean dynamics and being damped by the surface heat flux (not shown). Therefore, the combination of the dynamical and thermodynamically influences form the SSTA structure. Phase 3 (Fig. 11c) shows the demise of the negative SSTAs in the eastern equatorial IO, with mild warm SSTAs in most of the tropical basin. Corresponding to nearly negligible equatorial wind anomalies, the equatorial SSTA is particularly weak and the ocean and atmosphere are largely decoupled near the equator. In this phase, the equatorial ocean temperature anomalies are mostly subsurface around the thermocline (Figs. 9c and 10c), while the surface manifestation is at a minimum. In phase 4, associated with the basinwide deepening of the equatorial thermocline that is most significant in the east (Figs. 9d and 10d), SSTAs start to grow in the east (Fig. 11d). It is the initiation stage of the equatorial IO oscillation of the opposite phases.

The physical processes associated with this typical life cycle in the equatorial IO are similar to the RO paradigm of ENSO. It is characterized by the equilibrium (east–west asymmetry) and disequilibrium (east–west symmetry) of the upper-ocean heat content components. That is, the equatorial ocean heat content in the equatorial IO decreases before the positive IOD event, and increases after the peak. We have also noticed that the oscillation period is around 15 months, as shown in the

Brought to you by NOAA Central Library | Unauthenticated | Downloaded 07/19/23 05:04 PM UTC

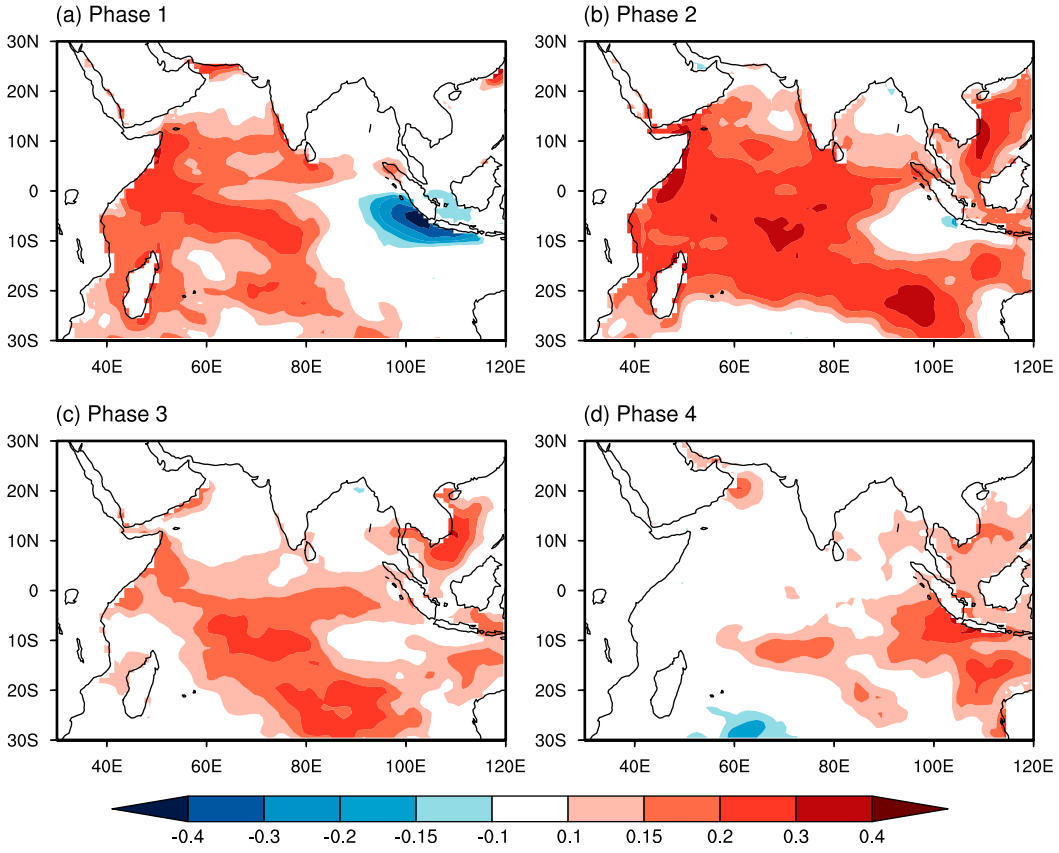

FIG. 11. The SSTA composites in phases (a) 1, (b) 2, (c) 3, and (d) 4. The unit of the SSTA is °C.

power spectrum of $c(t)$ (Fig. 7c). This is consistent with some previous studies that the IOD index exhibits a notable biennial component (e.g., Saji et al. 1999; Ashok et al. 2003) although a broad oscillation period of 2–5 years is generally observed (Huang and Kinter 2002; McPhaden and Nagura 2014). Our study shows that the oscillation is inherent of the equatorial IO with a quasi-periodicity around 15 months and the lower-frequency expansion in the observed IOD variability probably reflects the time scales of the external forcings such as ENSO.

c. *A nonlinear long-term warming trend in the Indian Ocean*

As we have discussed in section 3a, PC1 and PC3 contain apparent nonlinear long-term trends visually (Figs. 2d,f). These trends are delineated quantitatively in the EEMD analysis. Since the EEMD is adaptive, the trends are an intrinsically fitted monotonic function throughout the data span. Wu et al. (2007) argued that this approach is superior to those with extrinsic functions (e.g., linear trend) or predetermined parameters (moving mean). Since the variance of the trend of PC3 is much larger than the trend of PC1, we only focus on the trend of PC3 here. Figure 12a shows the upward nonlinear trend (red dashed curve) and linear trend (blue curve) superimposed on PC3 (black curve). Although the nonlinear trend is similar to the linear trend, the warming is slightly accelerating after 1983 (Fig. 12a). After removing the nonlinear trend, the detrended PC3 with high-frequency variability is also shown in Fig. 12b.

To explore how this nonlinear trend contributes to the spatial pattern of EOF3, its linear regressions with the upper-ocean temperature anomalies in 1958–2015 are presented in Fig. 12c. It can be seen that the trends of upper-ocean temperature anomalies along the equatorial IO vary vertically. There is a warming tendency above 100 m and a mild cooling one around 100–300 m (Fig. 12c), consistent with Barnett et al. (2005) and Pierce et al. (2006). In addition, the long-term trend in the eastern Indian Ocean is more significant than in the west and the maximum positive regression coefficients are around 80 m. Han et al. (2006) argued that this complex vertical structure exists mainly in the southern tropical and equatorial regions, because greenhouse gases heat up the ocean mixed layer temperature by increasing downward surface heat flux while the corresponding tropical wind anomalies increase the Ekman pumping, which shallows the thermocline. Such long-term trends of the subsurface ocean temperature may lead to the enhanced stratification of the equatorial IO. Although the vertical structure of the trend (Fig. 12c) bears a certain resemblance to the pattern of EOF3, it cannot explain the enhanced warming at 50–100 m centered at the central-western IO (Fig. 2c). In fact, the regression between the detrended PC3 and the upper-ocean temperature anomalies show a more similar pattern with EOF3 around 50–150 m in the central and

Brought to you by NOAA Central Library | Unauthenticated | Downloaded 07/19/23 05:04 PM UTC

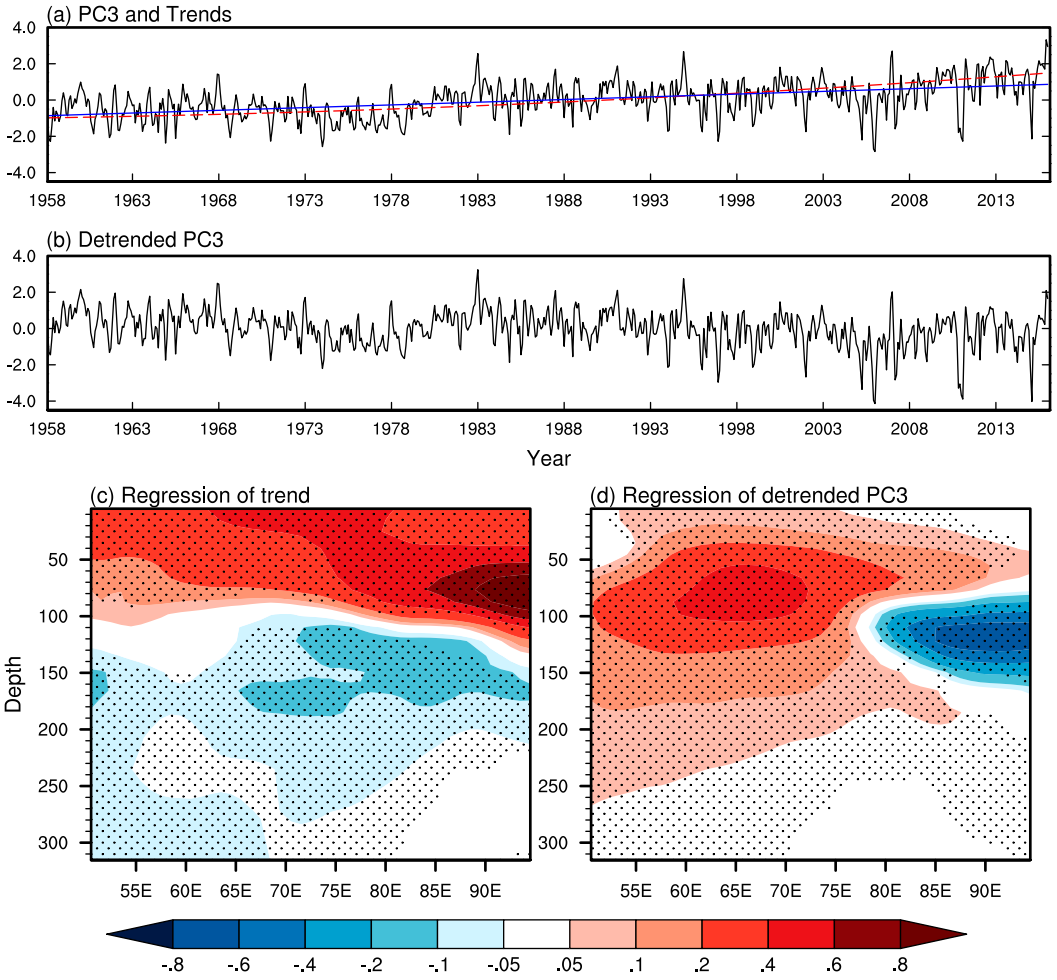

FIG. 12. (a) The original PC3 (black solid line) superimposed with the nonlinear trend (red dashed line) and linear trend (blue solid line) from 1985 to 2015 and (b) the detrended PC3 (the nonlinear trend is removed). Linear regression coefficients (c) between the nonlinear trend of PC3 and upper-ocean temperature anomalies and (d) between the detrended PC3 and upper-ocean temperature anomalies (unit: °C). Dotted areas indicate that the correlations coefficients are statistically significant above the 95% confidence level.

eastern IO (Fig. 12d). This indicates that the detrended fluctuation of PC3 is mostly associated with the adjustment of the thermocline slope, as well as the stratification in the thermocline zone. It seems to be distinguished from the trend by the much less changes in mixed layer temperature.

The trend and detrended fluctuation are also distinguished by their different basin connections. Figure 13a shows that all linear regression coefficients between SSTA and the nonlinear warming trend are positive throughout the IO basin, representing the continuing warming of the Indian Ocean. Compared with Fig. 13a, though weak negative regression coefficients emerge in the eastern equatorial IO and the southern IO when the trend of PC3 is removed, the maximum regression coefficients are still shown in the central equatorial IO (Fig. 13c). Unlike SSTA, HCA has obvious long-term warming south of 20°N and a slight warming trend along the equator and northeastern region, while it shows a cooling trend near 10°S (Fig. 13b). Also plotted on Fig. 13b are the linear regression coefficients between wind anomalies at the 10-m level and the nonlinear warming trend (vectors). The strengthening of equatorial westerly wind anomalies is conducive to eastern convergence and western divergence, resulting in warming of the eastern equatorial IO. This HCA pattern, including the cooling trend centered in the southwestern IO, is qualitatively similar to the SSHA trend simulated by an ocean general circulation model under observed surface forcing for 1961–2008 (Han et al. 2010, their Fig. 1), which corroborates with long-term tide gauge measurements well in several locations. The decreased HCA and the sea level drop are associated with the shoaling of the thermocline centered around the Seychelles ridge and increasing vertical stratification there, based on an examination of the observed temperature profiles in the historical archives (Alory et al. 2007). When the trend of PC3 is removed, the SSTA and HCA regression patterns become more dominated by equatorial-centered variations. The SSTA shows warm anomalies in the central equatorial IO (Fig. 13c) while the HCA pattern shows the contrast between the east and west, which is

Brought to you by NOAA Central Library | Unauthenticated | Downloaded 07/19/23 05:04 PM UTC

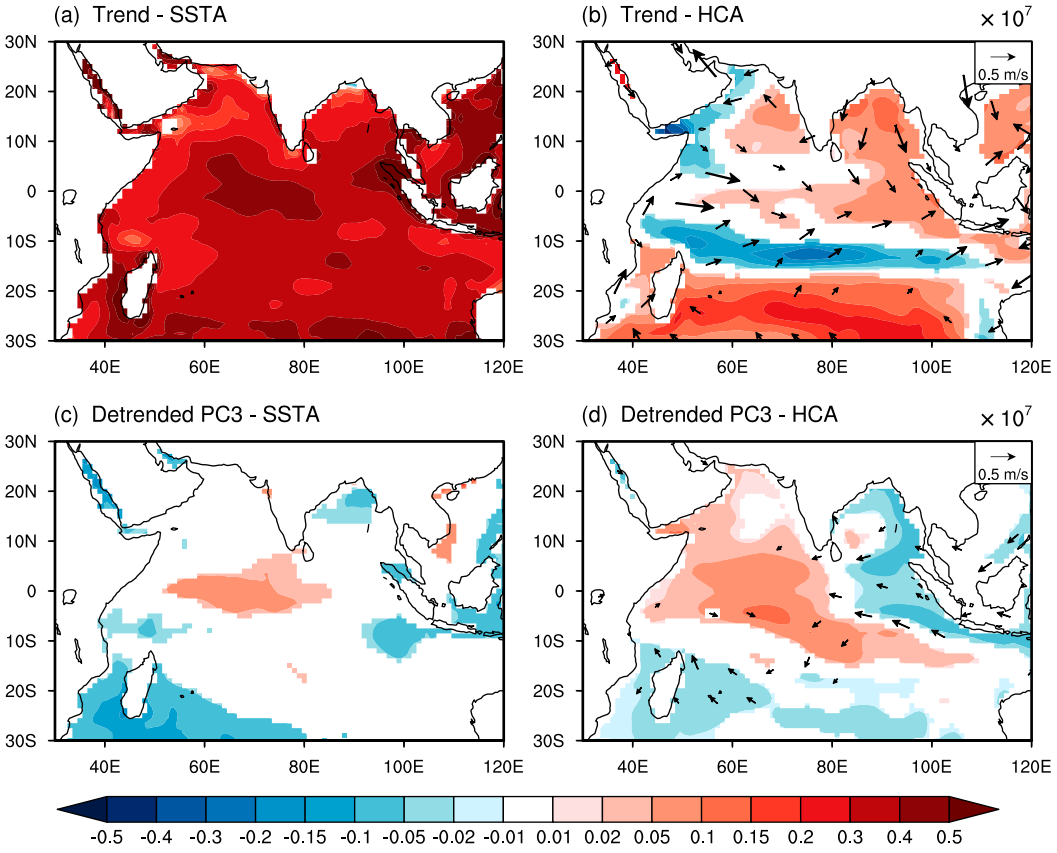

FIG. 13. Linear regression coefficients (a) between the nonlinear trend of PC3 and SSTA (shading; unit: °C), (b) between the nonlinear trend of PC3 and HCA (shading; unit: J m^{-2}) and between nonlinear trend of PC3 and 10-m wind anomalies (vectors; unit: m s^{-1}), (c) between the detrended PC3 and SSTA (shading; unit: °C), and (d) between the detrended PC3 and HCA (shading; unit: J m^{-2}) and between the detrended PC3 and 10-m wind anomalies (vectors; unit: m s^{-1}). All of the linear regression coefficients shown in this figure are statistically significant above the 95% confidence level.

associated with the easterly wind anomalies in the central and eastern equatorial IO (Fig. 13d). Although both patterns resemble certain phases of the equatorial IO oscillation discussed in section 3b, the meridional width of the equatorial anomalies is generally wider, suggesting that lower-frequency signals may be involved.

4. Summary and discussion

In this paper, we used a comprehensive ocean reanalysis for 1958–2015 to investigate the dominant patterns of interannual variability of the ocean temperature above 315 m in the equatorial IO. It is found that the three leading EOF modes, accounting for 70% of the total variance, characterize the major patterns of the temperature anomalies associated with the equatorial thermocline variations across the basin ranging from subannual to interannual time scales. An equatorial oscillation with a quasi-regular period around 15 months can be further identified from the coherent variations of the first two EOF modes on interannual bands. Consistent with the RO paradigm, this equatorial oscillation is characterized by the tilt mode of the thermocline in its peak phases and WWV mode in its transitional phases. The former is associated with an east–west SSTA dipole pattern while the latter corresponds to a displaced thermocline throughout the equatorial IO with little surface manifestation.

Although the basinwide HCA patterns bear a resemblance to the equatorial wave response to the equatorial wind forcing, we should be cautious in resorting to Kelvin waves as a quantitative explanation. In fact, equatorial oscillations with explicit Kelvin wave propagations occur in the subannual periods (e.g., Sengupta et al. 2007; Han et al. 2011). In comparison to these subannual oscillations, the HCAs in our composites are less symmetric with respect to the equator and less confined to the equatorial waveguide. In particular, the HCAs near 5°–10°S induced by wind stress curl in the midbasin provide slower westward-moving off-equatorial Rossby waves, which supply the warm water to recharge the equatorial zone after the positive IOD peak. In this sense, our results are consistent with the argument made by McPhaden and Nagura (2014) that the cycling of heat content between the off-equatorial (5°–10°S) and the equatorial zones keeps the biennial character of the

Brought to you by NOAA Central Library | Unauthenticated | Downloaded 07/19/23 05:04 PM UTC

IOD. This scenario of the IOD biennial tendency is different from the one proposed by some previous studies that considered it as an oceanic manifestation of the tropical biennial oscillation (TBO) (e.g., a weak monsoon year is followed by a strong monsoon year, and vice versa; Meehl 1993).

Stuecker et al. (2017) argued that the previously described biennial frequencies of IOD are actually a near-annual band when the monthly data are analyzed. Although this hints at the possible existence of a shorter time scale variation related to IOD, the physical mechanism we proposed for about 15-month variation of the upper-ocean heat content is totally different from the one they propose. Stuecker et al. (2017) explain the IOD variability as a response to stochastic, as well as external, forcings and argue that its observed near-annual band arises from the Indian Ocean response to the combination mode of ENSO–annual cycle interactions (C-mode; Stuecker et al. 2013). In this scenario, no oscillatory mechanism and oceanic memory are necessary within the Indian Ocean to generate the observed IOD events. In our scenario, this approximately 15-month variability arises from an intrinsic oscillation within the equatorial Indian Ocean, which forms the baseline of the IOD variability. That is why subsurface ocean observations in the tropical Indian Ocean seem to add skill to the IOD prediction (Doi et al. 2017).

On the other hand, since this intrinsic oscillation is somewhat damped, external forcings ranging from white-noise atmospheric disturbances to lower-frequency climate variability are crucial for the initial developments of specific events (e.g., Fedorov et al. 2003). These external forcings are most effective during certain phases of the internal oscillation, which may partly explain why major IOD events occur intermittently although the baseline oscillation is presumably continuous. Moreover, the ENSO forcing, having its own intrinsic frequencies that are lower than the Indian Ocean oscillation, also tends to enhance the lower-frequency band of the wide IOD spectrum.

In addition to the interannual oscillation, our study also identified a long-term nonlinear trend in the Indian Ocean. The upper-ocean temperature anomalies along the equatorial Indian Ocean are warming up above 100 m and cooling down around 100–300 m. The subsurface cooling occurs in a broader area centered in the southwestern equatorial Indian Ocean [also see, e.g., Han et al. (2010, their Fig. 7)]. Trenary and Han (2008) suggest that long-term changes in the surface winds over the tropical Indian Ocean caused the thermocline cooling. Some researchers also suggest that the SST warming trend in the equatorial IO is related to the changes observed in the summer monsoon circulation (Swapna et al. 2014). On the other hand, Alory et al. (2007) found that the reduced transport from the Indonesian Throughflow also played a major role, possibly caused by the weakened trade winds in the Pacific. Most studies agree that the long-term warming trend in the Indian Ocean is a manifestation of anthropogenic global warming (Barnett et al. 2005; Ihara et al. 2008). It is unclear how the atmospheric and oceanic circulations respond to the increase of greenhouse gas concentration that shaped its complicated temporal and spatial structure. That deserves further investigation. It is also noteworthy that there is uncertainty in the low-frequency variability of the datasets taken from the ORAS4, due to the discontinuity of temperature and forcings. Balmaseda et al. (2013) provided a detailed description of data assimilation and surface forcing in ORAS4. Moreover, we have yet to examine the multidecadal variations in the Indian Ocean, which are important not only in its own right but also in connecting the interannual variations with the long-term climate change. Last, our results are based on one ocean reanalysis and need to be corroborated by conducting similar analyses with different observational and/or reanalyzed ocean datasets.

Acknowledgments. This work was supported by the National Key R&D Program of China (2019YFA0606701) and Guangdong Major Project of Basic and Applied Basic Research (2020B0 301030004). B. Huang is supported by grants from NSF (AGS-1338427), NOAA (NA14OAR4310160 and NA17OAR4310144), and NASA (NNX14AM19G). We acknowledge the European Centre for Medium-Range Weather Forecasts for providing the Ocean Reanalysis System 4 (ORAS4) for this study.

REFERENCES

Allan, R. J., J. A. Lindesay, and C. J. C. Reason, 1995: Multidecadal variability in the climate system over the Indian Ocean region during the austral summer. *J. Climate*, **8**, 1853–1873, https://doi.org/10.1175/1520-0442(1995)008<1853:MVITCS>2.0.CO;2.

Alory, G., S. Wijffels, and G. Meyers, 2007: Observed temperature trends in the Indian Ocean over 1960–1999 and associated mechanisms. *Geophys. Res. Lett.*, **34**, L02606, https://doi.org/10.1029/2006GL028044.

Annamalai, H., and R. Murtugudde, 2004: *Earth's Climate. Geophys. Monogr.*, Vol. 147, Amer. Geophys. Union, 213–246, https://doi.org/10.1029/147GM13.

Ashok, K., Z. Guan, and T. Yamagata, 2003: A look at the relationship between the ENSO and the Indian Ocean dipole. *J. Meteor. Soc. Japan*, **81**, 41–56, https://doi.org/10.2151/jmsj.81.41.

Balmaseda, M. A., K. Mogensen, and A. T. Weaver, 2013: Evaluation of the ECMWF Ocean Reanalysis System ORAS4. *Quart. J. Roy. Meteor. Soc.*, **139**, 1132–1161, https://doi.org/10.1002/qj.2063.

Barnett, T., D. Pierce, K. Achutarao, P. Gleckler, B. Santer, J. Gregory, and W. Washington, 2005: Penetration of human-induced warming into the world's oceans. *Science*, **309**, 284–287, https://doi.org/10.1126/science.1112418.

Barnston, A. G., M. Chelliah, and S. B. Goldenberg, 1997: Documentation of a highly ENSO-related SST region in the equatorial Pacific: Research note. *Atmos. Ocean*, **35**, 367–383, https://doi.org/10.1080/07055900.1997.9649597.

Cane, M. A., and S. E. Zebiak, 1985: A theory for El Niño and the Southern Oscillation. *Science*, **228**, 1085–1087, https://doi.org/10.1126/science.228.4703.1085.

Chambers, D. P., B. D. Tapley, and R. H. Stewart, 1999: Anomalous warming in the Indian Ocean coincident with El Niño. *J. Geophys. Res.*, **104**, 3035–3047, https://doi.org/10.1029/1998JC900085.

Chu, J.-E., K.-J. Ha, J.-Y. Lee, B. Wang, B.-H. Kim, and C. E. Chung, 2014: Future change of the Indian Ocean basin-wide and dipole modes in the CMIP5. *Climate Dyn.*, **43**, 535–551, https://doi.org/10.1007/s00382-013-2002-7.

Clarke, A. J., 2010: Analytical theory for the quasi-steady and low-frequency equatorial ocean response to wind forcing: The

Brought to you by NOAA Central Library | Unauthenticated | Downloaded 07/19/23 05:04 PM UTC

"tilt" and "warm water volume" modes. *J. Phys. Oceanogr.*, **40**, 121–137, https://doi.org/10.1175/2009JPO4263.1.

Doi, T., A. Storto, S. K. Behera, A. Navarra, and T. Yamagata, 2017: Improved prediction of the Indian Ocean dipole mode by use of subsurface ocean observations. *J. Climate*, **30**, 7953–7970, https://doi.org/10.1175/JCLI-D-16-0915.1.

Fedorov, A. V., S. L. Harper, S. G. Philander, B. Winter, and A. Wittenberg, 2003: How predictable is El Niño? *Bull. Amer. Meteor. Soc.*, **84**, 911–920, https://doi.org/10.1175/BAMS-84-7-911.

Feng, J., Z. Wu, and G. Liu, 2014: Fast multidimensional ensemble empirical mode decomposition using a data compression technique. *J. Climate*, **27**, 3492–3504, https://doi.org/10.1175/JCLI-D-13-00746.1.

Feng, M., and G. Meyers, 2003: Interannual variability in the tropical Indian Ocean: A two-year time-scale of Indian Ocean dipole. *Deep-Sea Res. II*, **50**, 2263–2284, https://doi.org/10.1016/S0967-0645(03)00056-0.

——, ——, and S. Wijffels, 2001: Interannual upper ocean variability in the tropical Indian Ocean. *Geophys. Res. Lett.*, **28**, 4151–4154, https://doi.org/10.1029/2001GL013475.

Fischer, A. S., P. Terray, E. Guilyardi, S. Gualdi, and P. Delecluse, 2005: Two independent triggers for the Indian Ocean dipole/zonal mode in a coupled GCM. *J. Climate*, **18**, 3428–3449, https://doi.org/10.1175/JCLI3478.1.

Gill, A. E., 1982: *Atmosphere–Ocean Dynamics*. Academic Press, 662 pp.

Guo, F., Q. Liu, J. Yang, and L. Fan, 2018: Three types of Indian Ocean Basin modes. *Climate Dyn.*, **51**, 4357–4370, https://doi.org/10.1007/s00382-017-3676-z.

Han, W., G. A. Meehl, and A. Hu, 2006: Interpretation of tropical thermocline cooling in the Indian and Pacific Oceans during recent decades. *Geophys. Res. Lett.*, **33**, L23615, https://doi.org/10.1029/2006GL027982.

——, and Coauthors, 2010: Patterns of Indian Ocean sea-level change in a warming climate. *Nat. Geosci.*, **3**, 546–550, https://doi.org/10.1038/ngeo901.

——, J. P. McCreary, Y. Masumoto, J. Vialard, and B. Duncan, 2011: Basin resonances in the equatorial Indian Ocean. *J. Phys. Oceanogr.*, **41**, 1252–1270, https://doi.org/10.1175/2011JPO4591.1.

——, J. Vialard, M. J. McPhaden, T. Lee, Y. Masumoto, M. Feng, and W. P. M. Ruijter, 2014: Indian Ocean decadal variability: A review. *Bull. Amer. Meteor. Soc.*, **95**, 1679–1703, https://doi.org/10.1175/BAMS-D-13-00028.1.

Hu, Z.-Z., A. Kumar, B. Huang, and J. Zhu, 2013: Leading modes of the upper-ocean temperature interannual variability along the equatorial Atlantic Ocean in NCEP GODAS. *J. Climate*, **26**, 4649–4663, https://doi.org/10.1175/JCLI-D-12-00629.1.

——, ——, J. Zhu, B. Huang, Y. Tseng, and X. Wang, 2017: On the shortening of the lead time of ocean warm water volume to ENSO SST since 2000. *Sci. Rep.*, **7**, 4294, https://doi.org/10.1038/s41598-017-04566-z.

Huang, B., and J. L. Kinter, 2002: Interannual variability in the tropical Indian Ocean. *J. Geophys. Res.*, **107**, 3199, https://doi.org/10.1029/2001JC001278.

——, and J. Shukla, 2007a: Mechanisms for the interannual variability in the tropical Indian Ocean. Part I: The role of remote forcing from the tropical Pacific. *J. Climate*, **20**, 2917–2936, https://doi.org/10.1175/JCLI4151.1.

——, and ——, 2007b: Mechanisms for the interannual variability in the tropical Indian Ocean. Part II: Regional processes. *J. Climate*, **20**, 2937–2960, https://doi.org/10.1175/JCLI4169.1.

——, Z.-Z. Hu, J. L. Kinter, Z. Wu, and A. Kumar, 2012: Connection of stratospheric QBO with global atmospheric general circulation and tropical SST. Part I: Methodology and composite life cycle. *Climate Dyn.*, **38** (1–2), 1–23, https://doi.org/10.1007/s00382-011-1250-7.

Huang, N. E., and Z. Wu, 2008: A review on Hilbert-Huang transform: Method and its applications to geophysical studies. *Rev. Geophys.*, **46**, RG2006, https://doi.org/10.1029/2007RG000228.

——, Z. Shen, S. R. Long, M. C. Wu, E. H. Shih, Q. Zheng, C. C. Tung, and H. H. Liu, 1998: The empirical mode decomposition and the Hilbert spectrum for nonlinear and non-stationary time series analysis. *Proc. Roy. Soc. London*, **454**, 903–995, https://doi.org/10.1098/rspa.1998.0193.

Ihara, C., Y. Kushnir, and M. A. Cane, 2008: Warming trend of the Indian Ocean SST and Indian Ocean dipole from 1880 to 2004. *J. Climate*, **21**, 2035–2046, https://doi.org/10.1175/2007JCLI1945.1.

Iskandar, I., W. Mardiansyah, Y. Masumoto, and T. Yamagata, 2005: Intraseasonal Kelvin waves along the southern coast of Sumatra and Java. *J. Geophys. Res*, **110**, C04013, https://doi.org/10.1029/2004JC002508.

Jansen, M. F., D. Dommenget, and N. Keenlyside, 2009: Tropical atmosphere–ocean interactions in a conceptual framework. *J. Climate*, **22**, 550–567, https://doi.org/10.1175/2008JCLI2243.1.

Jin, F.-F., 1997: An equatorial ocean recharge paradigm for ENSO. Part I: Conceptual model. *J. Atmos. Sci.*, **54**, 811–829, https://doi.org/10.1175/1520-0469(1997)054<0811:AEORPF>2.0.CO;2.

Jury, M. R., and B. Huang, 2004: The Rossby wave as a key mechanism of Indian Ocean climate variability. *Deep-Sea Res. I*, **51**, 2123–2136, https://doi.org/10.1016/j.dsr.2004.06.005.

Kalnay, E., and Coauthors, 1996: The NCEP/NCAR 40-Year Reanalysis Project. *Bull. Amer. Meteor. Soc.*, **77**, 437–471, https://doi.org/10.1175/1520-0477(1996)077<0437:TNYRP>2.0.CO;2.

Kawamura, R., 1994: A rotated EOF analysis of global sea surface temperature variability with interannual and interdecadal scales. *J. Phys. Oceanogr.*, **24**, 707–715, https://doi.org/10.1175/1520-0485(1994)024<0707:AREAOG>2.0.CO;2.

Klein, S. A., B. J. Soden, and N.-C. Lau, 1999: Remote sea surface temperature variations during ENSO: Evidence for a tropical atmospheric bridge. *J. Climate*, **12**, 917–932, https://doi.org/10.1175/1520-0442(1999)012<0917:RSSTVD>2.0.CO;2.

Kumar, A., and Z.-Z. Hu, 2014: Interannual and interdecadal variability of ocean temperature along the equatorial Pacific in conjunction with ENSO. *Climate Dyn.*, **42**, 1243–1258, https://doi.org/10.1007/s00382-013-1721-0.

Lanzante, J. R., 1996: Lag relationships involving tropical sea surface temperatures. *J. Climate*, **9**, 2568–2578, https://doi.org/10.1175/1520-0442(1996)009<2568:LRITSS>2.0.CO;2.

Lau, K.-H., and N.-C. Lau, 1990: Observed structure and propagation characteristics of tropical summertime synoptic scale disturbances. *Mon. Wea. Rev.*, **118**, 1888–1913, https://doi.org/10.1175/1520-0493(1990)118<1888:OSAPCO>2.0.CO;2.

Levitus, S., J. I. Antonov, T. P. Boyer, R. A. Locarnini, H. E. Garcia, and A. V. Mishonov, 2009: Global ocean heat content 1955–2008 in light of recently revealed instrumentation problems. *Geophys. Res. Lett.*, **36**, L07608, https://doi.org/10.1029/2008GL037155.

Li, D.-H., M. Zhang, G. Zhang, and Y.-K. Tan, 2005: The study of the occurrence and evolution mechanism of the tropical Indian Ocean dipole (in Chinese). *Adv. Mar. Sci.*, **23**, 135–143.

Masumoto, Y., and G. Meyers, 1998: Forced Rossby waves in the southern tropical Indian Ocean. *J. Geophys. Res.*, **103**, 27 589–27 602, https://doi.org/10.1029/98JC02546.

Brought to you by NOAA Central Library | Unauthenticated | Downloaded 07/19/23 05:04 PM UTC

McPhaden, M. J., and M. Nagura, 2014: Indian Ocean dipole interpreted in terms of recharge oscillator theory. *Climate Dyn.*, **42**, 1569–1586, https://doi.org/10.1007/s00382-013-1765-1.

Meehl, G. A., 1993: A coupled air–sea biennial mechanism in the tropical Indian and Pacific regions: Role of the ocean. *J. Climate*, **6**, 31–41, https://doi.org/10.1175/1520-0442(1993)006<0031:ACASBM>2.0.CO;2.

Meinen, C. S., and M. J. McPhaden, 2000: Observations of warm water volume changes in the equatorial Pacific and their relationship to El Niño and La Niña. *J. Climate*, **13**, 3551–3559, https://doi.org/10.1175/1520-0442(2000)013<3551:OOWWVC>2.0.CO;2.

Meyers, G., P. McIntosh, L. Pigot, and M. Pook, 2007: The years of El Niño, La Niña, and interactions with the tropical Indian Ocean. *J. Climate*, **20**, 2872–2880, https://doi.org/10.1175/JCLI4152.1.

Moron, V., R. Vautard, and M. Ghil, 1998: Trends, interdecadal and interannual oscillations in global sea-surface temperatures. *Climate Dyn.*, **14**, 545–569, https://doi.org/10.1007/s003820050241.

Neelin, J. D., 1991: The slow sea surface temperature mode and the fast-wave limit: Analytic theory for tropical interannual oscillations and experiments in a hybrid coupled model. *J. Atmos. Sci.*, **48**, 584–606, https://doi.org/10.1175/1520-0469(1991)048<0584:TSSSTM>2.0.CO;2.

Nicholson, S. E., 1997: An analysis of the ENSO signal in the tropical Atlantic and western Indian Oceans. *Int. J. Climatol.*, **17**, 345–375, https://doi.org/10.1002/(SICI)1097-0088(19970330)17:4<345::AID-JOC127>3.0.CO;2-3.

North, G. R., T. L. Bell, R. F. Cahalan, and F. J. Moeng, 1982: Sampling errors in the estimation of empirical orthogonal functions. *Mon. Wea. Rev.*, **110**, 699–706, https://doi.org/10.1175/1520-0493(1982)110<0699:SEITEO>2.0.CO;2.

Padmanabhan, G., and A. R. Rao, 1986: Maximum entropy spectra of some rainfall and river flow time series from southern and central India. *Theor. Appl. Climatol.*, **37**, 63–73, https://doi.org/10.1007/BF00866105.

Pan, Y. H., and A. H. Oort, 1990: Correlation analyses between sea surface temperature anomalies in the eastern equatorial Pacific and the world ocean. *Climate Dyn.*, **4**, 191–205, https://doi.org/10.1007/BF00209521.

Philander, S. G., 1990: *El Niño, La Niña, and the Southern Oscillation*. Academic Press, 293 pp.

Pierce, D. W., T. P. Barnett, K. M. AchutaRao, P. J. Gleckler, J. M. Gregory, and W. M. Washington, 2006: Anthropogenic warming of the oceans: Observations and model results. *J. Climate*, **19**, 1873–1900, https://doi.org/10.1175/JCLI3723.1.

Qian, C., C. Fu, Z. Wu, and Z. Yan, 2011: The role of changes in the annual cycle in earlier onset of climatic spring in northern China. *Adv. Atmos. Sci.*, **28**, 284–296, https://doi.org/10.1007/s00376-010-9221-1.

Rao, S., S. Behera, Y. Masumoto, and T. Yamagata, 2002: Interannual subsurface variability in the tropical Indian Ocean with a special emphasis on the Indian Ocean Dipole. *Deep-Sea Res. II*, **49**, 1549–1572, https://doi.org/10.1016/S0967-0645(01)00158-8.

Ren, N. X., and Z. L. Liu, 2018: Spectrum analysis based on modern signal processing. *Comput. Eng. Software*, **39**, 157–159, https://doi.org/10.3969/j.issn.1003-6970.2018.03.035.

Ren, R., S. Sun, Y. Yang, and Q. Li, 2015: Summer SST anomalies in the Indian Ocean and the seasonal timing of ENSO decay phase. *Climate Dyn.*, **47**, 1827–1844, https://doi.org/10.1007/S00382-015-2935-0.

Saji, N. H., B. N. Goswami, P. Vinayachandran, and T. Yamagata, 1999: A dipole mode in the tropical Indian Ocean. *Nature*, **401**, 360–363, https://doi.org/10.1038/43854.

Schneider, E. K., B. Huang, and J. Shukla, 1995: Ocean wave dynamics and El Niño. *J. Climate*, **8**, 2415–2439, https://doi.org/10.1175/1520-0442(1995)008<2415:OWDAEN>2.0.CO;2.

Schott, F. A., and J. McCreary, 2001: The monsoon circulation of the Indian Ocean. *Prog. Oceanogr.*, **51** (1), 1–123, https://doi.org/10.1016/S0079-6611(01)00083-0.

——, S.-P. Xie, and J. P. McCreary Jr., 2009: Indian Ocean circulation and climate variability. *Rev. Geophys.*, **47**, RG1002, https://doi.org/10.1029/2007RG000245.

Sengupta, D., R. Senan, B. N. Goswami, and J. Vialard, 2007: Intraseasonal variability of equatorial Indian Ocean zonal currents. *J. Climate*, **20**, 3036–3055, https://doi.org/10.1175/JCLI4166.1.

Stuecker, M. F., A. Timmermann, F.-F. Jin, S. McGregor, and H. L. Ren, 2013: A combination mode of the annual cycle and the El Niño/Southern Oscillation. *Nat. Geosci.*, **6**, 540–544, https://doi.org/10.1038/ngeo1826.

——, ——, ——, Y. Chikamoto, W. Zhang, A. T. Wittenberg, E. Widiasih, and S. Zhao, 2017: Revisiting ENSO/Indian Ocean dipole phase relationships. *Geophys. Res. Lett.*, **44**, 2481–2492, https://doi.org/10.1002/2016GL072308.

Swapna, P., R. Krishnan, and J. M. Wallace, 2014: Indian Ocean and monsoon coupled interactions in a warming environment. *Climate Dyn.*, **42**, 2439–2454, https://doi.org/10.1007/s00382-013-1787-8.

Tan, Y., R. Zhang, and J. He, 2003: Features of the interannual variation of sea surface temperature anomalies and the air–sea interaction in tropical IndianOcean (in Chinese). *Chin. J. Atmos. Sci.*, **27**, 53–66.

Terray, P., and S. Dominiak, 2005: Indian Ocean sea surface temperature and El Niño–Southern Oscillation: A new perspective. *J. Climate*, **18**, 1351–1368, https://doi.org/10.1175/JCLI3338.1.

Tourre, Y. M., and W. B. White, 1997: Evolution of the ENSO signal over the Indo–Pacific domain. *J. Phys. Oceanogr.*, **27**, 683–696, https://doi.org/10.1175/1520-0485(1997)027<0683:EOTESO>2.0.CO;2.

Trenary, L., and W. Han, 2008: Causes of decadal subsurface cooling in the tropical Indian Ocean during 1961–2000. *Geophys. Res. Lett.*, **35**, L17602, https://doi.org/10.1029/2008GL034687.

Venzke, S., M. Latif, and A. Villwock, 2000: The coupled GCM ECHO-2. *J. Climate*, **13**, 1371–1383, https://doi.org/10.1175/1520-0442(2000)013<1371:TCGE>2.0.CO;2.

Wang, C., 2019: Three-ocean interactions and climate variability: A review and perspective. *Climate Dyn.*, **53**, 5119–5136, https://doi.org/10.1007/s00382-019-04930-x.

Webster, P., A. Moore, J. Loschnigg, and R. Leben, 1999: Coupled ocean–atmosphere dynamics in the Indian Ocean during 1997-98. *Nature*, **401**, 356–360, https://doi.org/10.1038/43848.

Wu, Y., and B.-W. Shen, 2016: An evaluation of the parallel ensemble empirical mode decomposition method in revealing the role of downscaling processes associated with African easterly waves in tropical cyclone genesis. *J. Atmos. Oceanic Technol.*, **33**, 1611–1628, https://doi.org/10.1175/JTECH-D-15-0257.1.

——, and Y. Tang, 2019: Seasonal predictability of the tropical Indian Ocean SST in the North American Multimodel Ensemble. *Climate Dyn.*, **53**, 3361–3372, https://doi.org/10.1007/s00382-019-04709-0.

Wu, Z., and N. E. Huang, 2009: Ensemble empirical mode decomposition: A noise-assisted data analysis method. *Adv. Adapt. Data Anal.*, **1** (1), 1–41, https://doi.org/10.1142/S1793536909000047.

Brought to you by NOAA Central Library | Unauthenticated | Downloaded 07/19/23 05:04 PM UTC

——, N. Huang, S. Long, and C.-K. Peng, 2007: On the trend, detrending, and variability of nonlinear and nonstationary time series. *Proc. Natl. Acad. Sci. USA*, **104**, 14 889–14 894, https://doi.org/10.1073/pnas.0701020104.

Wyrtki, K., 1973: An equatorial jet in the Indian Ocean. *Science*, **181**, 262–264, https://doi.org/10.1126/science.181.4096.262.

——, 1975: Fluctuations of the dynamic topography in the Pacific Ocean. *J. Phys. Oceanogr.*, **5**, 450–459, https://doi.org/10.1175/1520-0485(1975)005<0450:FOTDTI>2.0.CO;2.

Xie, S.-P., H. Annamalai, F. A. Schott, and J. P. McCreary, 2002: Structure and mechanisms of south Indian Ocean climate variability. *J. Climate*, **15**, 864–878, https://doi.org/10.1175/1520-0442(2002)015<0864:SAMOSI>2.0.CO;2.

——, Y. Kosaka, Y. Du, K. Hu, J. S. Chowdary, and G. Huang, 2016: Indo-western Pacific Ocean capacitor and coherent climate anomalies in post-ENSO summer: A review. *Adv. Atmos. Sci.*, **33**, 411–432, https://doi.org/10.1007/s00376-015-5192-6.

Yamagata, T., S. Behera, J.-J. Luo, S. Masson, M. Jury, and S. Rao, 2004: Coupled ocean–atmosphere variability in the tropical Indian Ocean. *Earth's Climate: The Ocean–Atmosphere Interaction. Geophys. Monogr.*, Vol. 147, Amer. Geophys. Union, 189–212.

Yang, J., Q. Liu, S.-P. Xie, Z. Liu, and L. Wu, 2007: Impact of Indian Ocean SST basin mode on the Asian summer monsoon. *Geophys. Res. Lett.*, **34**, L02708, https://doi.org/10.1029/2006GL028571.

Zhang, X., and W. Han, 2020: Effects of climate modes on interannual variability of upwelling in the tropical Indian Ocean. *J. Climate*, **33**, 1547–1573, https://doi.org/10.1175/JCLI-D-19-0386.1.

Zhang, Y. Z., J. P. Li, J. Q. Xue, J. Feng, Q. Y. Wang, Y. D. Xu, and Y. H. Wang, 2018: Impact of the South China Sea summer monsoon on the Indian Ocean dipole. *J. Climate*, **31**, 6557–6573, https://doi.org/10.1175/JCLI-D-17-0815.1.

Zhu, J., B. Huang, A. Kumar, and J. L. Kinter III, 2015: Seasonality in prediction skill and predictable pattern of tropical Indian Ocean SST. *J. Climate*, **28**, 7962–7984, https://doi.org/10.1175/JCLI-D-15-0067.1.

Brought to you by NOAA Central Library | Unauthenticated | Downloaded 07/19/23 05:04 PM UTC